Optical and X-ray properties of the RIXOS AGN: I - The continua

E. M. Puchnarewicz,[1] K. O. Mason,[1] E. Romero-Colmenero,[1] F. J. Carrera,[1]
G. Hasinger,[2] R. McMahon,[3] J. P. D. Mittaz,[1] M. J. Page[1] and R. Carballo[4,5]

[1] *Mullard Space Science Laboratory, University College London, Holmbury St. Mary, Dorking, Surrey RH5 6NT, UK.*
[2] *Astrophysikalisches Institut Potsdam, An der Sternwarte 16, Potsdam, Germany.*
[3] *Institute of Astronomy, Madingley Road, Cambridge CB3 0HA, UK.*
[4] *Instituto de Fisica de Cantabria, Avda. de los Castros s/n 39005, Santander, Spain.*
[5] *Dept. Fisica Moderna, Universidad de Cantabria, Avda. de los Castros s/n 39005, Santander, Spain.*

ABSTRACT

We present measurements of the optical and X-ray continua of 108 AGN (Seyfert 1s and quasars) from the Rosat International X-ray/Optical Survey (RIXOS). The sample covers a wide range in redshift ($0 < z < 3.3$), in X-ray spectral slope ($-1.5 < \alpha_{\rm x} < 2.6$) and in optical-to-X-ray ratio ($0.4 < \alpha_{\rm ox} < 1.5$). A correlation is found between $\alpha_{\rm x}$ and $\alpha_{\rm ox}$; similar correlations have recently been reported in other X-ray and optical samples. We also identify previously unreported relationships between the optical slope ($\alpha_{\rm opt}$) and $\alpha_{\rm x}$ (particularly at high redshifts) and between $\alpha_{\rm opt}$ and $\alpha_{\rm ox}$. These trends show that the overall optical-to-X-ray continuum changes from convex to concave as $\alpha_{\rm x}$ hardens, demonstrating a strong behavioural link between the optical/UV big blue bump (BBB) and the soft X-ray excess, which is consistent with them being part of the same spectral component.

By constructing models of the optical-to-X-ray continuum, we demonstrate that the observed correlations are consistent with an intrinsic spectrum which is absorbed through different amounts of cold gas and dust. The intrinsic spectrum is the sum of an optical-to-soft X-ray 'big bump' component and an $\alpha_{\rm x}=1$ power law; the column density of the cold gas ranges from 0 to $\sim 4 \times 10^{21}$ cm^{-2} and the dust-to-gas ratio is assumed to be Galactic. The 'big bump' may be represented by a $T_{\rm brem} \sim 10^6$K thermal bremsstrahlung or an accretion disk with a surrounding hot corona. The scatter in the data can accommodate a wide range in big bump temperature (or black hole mass) and strength. A source for the absorbing gas may be the dusty, molecular torus which lies beyond the broad line-emitting regions, although with a much lower column density than observed in Seyfert 2 galaxies. Alternatively, it may be the bulge of a spiral host galaxy or an elliptical host galaxy.

Key words: Quasars: general – Galaxies: Active – Galaxies: Seyfert – X-rays: general.

1 INTRODUCTION

Three major continuum components are observed in the optical-to-X-ray spectra of non-blazar AGN; the big blue bump (BBB), which rises through the optical and UV (e.g. Edelson & Malkan 1986; Elvis et al. 1994), the 'canonical' hard X-ray power-law, which dominates above ~ 2 keV (e.g. Mushotzky 1984; Turner & Pounds 1989; Comastri et al. 1992) and the soft X-ray ($E < 1.0$ keV) 'excess' above the X-ray power-law [e.g. Arnaud et al. 1985; Turner & Pounds 1989; Walter & Fink 1993 (hereafter WF)]. The BBB generally dominates the bolometric luminosity of non-blazar AGN spectra and the soft X-ray excess may be its high energy tail. The variability of the BBB indicates that it is emitted from the nuclear regions of AGN (e.g. Clavel et al. 1991) and a popular model is that of blackbody-like emission from an optically-thick accretion disc (AD; e.g. Sun & Malkan 1989; Czerny & Elvis 1987; Madau 1988).

Measurements of the BBB's spectral form, and consequently model development, are limited however because the peak of the BBB, and much of its frequency coverage are lost in the EUV where only a handful of AGN may be detected. Nonetheless, using UV and soft X-ray data from X-ray bright Seyferts, WF reported a correlation between the 1375 Å-to-2 keV flux ratio and the slope of the soft X-ray (0.2-2.0 keV) spectrum, in the sense that AGN with relatively soft X-ray spectra also have a high UV-to-X-ray ratio. They suggested that the correlation was due to changes in the flux of a single optical-to-soft X-ray 'big bump' relative to an underlying continuum. Laor et al. (1994; hereafter L94) have reported a similar correlation in their sample of UV-excess quasars. This has provided the first direct evidence of a link between the BBB and the soft X-ray excess, although there still remains doubt as to whether they are the same component, or separate but related (Fiore et al. 1995).

One restriction of the three samples mentioned previ-

ously (i.e. WF, L94 and Fiore et al. 1995) is that they are dominated by low-redshift ($z < 0.4$) AGN whose properties may differ from relatively high-luminosity quasars. The L94 sample is made up of nearby ($z \leq 0.4$) quasars with strong, blue optical/UV continua and the Fiore AGN have a relatively high optical-to-hard-X-ray (2500 Å-to-2 keV) luminosity ratio; these criteria favour AGN with strong BBBs. The WF sample contains 58 soft X-ray (0.08-2.4 keV) bright Seyferts which may also favour AGN with strong BBBs. A sample of AGN which spans a wider range in X-ray slope and optical to X-ray ratio would be better suited to a more thorough investigation of the soft X-ray excess and the optical/UV BBB.

We have used AGN (i.e. the Seyfert 1s and quasars) detected as part of the RIXOS survey (Mason et al. 1996) to extend this research. The RIXOS survey, which is described in Section 2, is made up of serendipitous sources detected in long-exposure pointed observations made with the *ROSAT* Position Sensitive Proportional Counter (PSPC; Pfeffermann et al. 1986). RIXOS sources are selected according to their flux *above* 0.4 keV, thereby reducing the preference for AGN with a strong soft X-ray excess. They cover a wide range in redshift ($0 < z < 3.3$), X-ray spectral slope ($-1.5 < \alpha_x < 2.6$) and in the optical-to-X-ray flux ratio ($0.4 < \alpha_{ox} < 1.5$), providing an extensive coverage of parameter space in which to search for trends and correlations.

In Section 2 we outline the essential details of the survey and the process for extracting and measuring the X-ray and optical data. The overall properties of the sample, correlations and 'mean' optical-to-X-ray spectra are presented in Section 3 while in Section 4 we present a model for the RIXOS AGN continua. The implications for the big bump and for the structure and geometry of AGN are discussed in Section 5.

In total, 108 AGN are included in this analysis; the full source list giving X-ray and optical positions, fluxes etc., will be presented in a future paper (Mason et al. 1996) when the survey is complete. A companion paper to this (Puchnarewicz et al. 1996) will discuss the relationships between the optical and UV lines and the continuum parameters.

2　THE RIXOS SURVEY

The RIXOS survey is compiled from serendipitous sources detected in pointed PSPC observations. To be included in the survey, an observation must have an exposure time of at least 8 ksec and it must have been taken at a Galactic latitude greater than $28°$ (where the Galactic absorbing column density is low). Only sources within 17 arcmin of the centre of the field and with a flux greater than 3×10^{-14} erg sec^{-1} in the *ROSAT* 'hard' band (0.4-2.0 keV) are used. These criteria ensure that source selection is made irrespective of the strength of any soft X-ray excess which dominates at low energies ($E < 0.5$ keV), however by ignoring any counts below 0.4 keV, there will be a bias against ultrasoft X-ray AGN like E 1346+266 and RE J1034+396 (Puchnarewicz, Mason & Córdova 1994; Puchnarewicz et al. 1995), which have relatively little flux in the 'hard' band. Most sources lie behind relatively low Galactic N_H (N_{HGal}), 60 per cent of the RIXOS AGN have an $N_{HGal} \leq 2 \times 10^{20}$ cm^{-2} and all have an N_{HGal} below 5×10^{20} cm^{-2}.
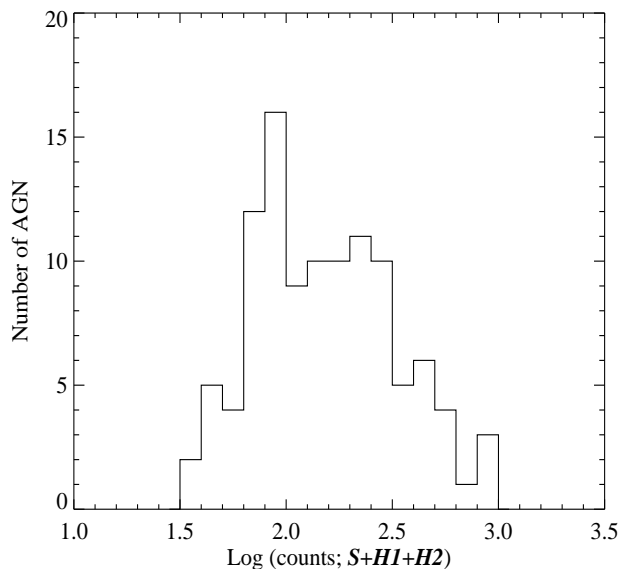

Figure 1. The distribution of total source counts for the spectra used in this analysis

The RIXOS survey is 100% complete over 20 sq degrees to a flux of 8.4×10^{-14} erg cm^{-2} s^{-1} and 93% complete over 15 sq degrees to a flux of 3×10^{-14} erg cm^{-2} s^{-1} (Mason et al. 1996). The subsample analysed for this paper is drawn from the first objects to be identified from the whole survey: confused sources (i.e. those which were less than 30 arcsec from other RIXOS sources), sources with poorly constrained fits to the X-ray data and objects with very weak optical spectra have been discarded. We find no significant differences between the X-ray parameters of the AGN presented here and those from the 100% complete sample (see Mittaz et al. 1996), thus we expect that the properties of this subsample are representative of the final survey.

2.1　X-ray data

To measure the X-ray spectral distribution of each source, the PSPC counts are divided into three bands, *S* (0.1 to 0.4 keV; channels 8 to 41), *H1* (0.5 to 0.9 keV; channels 52 to 90) and *H2* (0.9 to 2.0 keV; channels 91 to 201). At the first stage in the reduction process, periods of high count rate in the time series of the background were removed. The source signal in each band was measured by summing the counts in a circle centred on the source's centroid position: in most cases the radius of the extraction circle was 54 arcsec, however where other sources lay closer than 54 arcsec, a circle with a radius of one-half of the distance between the source and its nearest neighbour was used (in these cases, extraction radii are indicated in column 2 of Table 1). The 54 arcsec radius was chosen by simulation to optimize the signal-to-background ratio for the generally faint sources in the RIXOS survey. All source fluxes were corrected for counts falling outside the extraction circle using the formulae in Hasinger et al. (1994), out to a radius of 3 arcmin. A large, annular region, centred on the pointing position of the field, was used to calculate a model for the background, after correcting for vignetting and having masked out any source emission.

The broadband measurements were combined to produce 'spectra' with three data points for each source. A histogram illustrating the distribution of the total counts in the sources used in the present analysis is plotted in Fig 1 and shows that one half have at least 150 counts. The '3-colour' X-ray spectra were fitted using single power-law models, fixing the absorption to the Galactic column density [this was calculated by interpolating between the 21 cm measurements of Stark et al. (1992)]. With two free parameters (power-law index and normalization), this left one degree of freedom for the fits.

Many of the RIXOS sources have less than 15 counts in at least one of the *S, H1* or *H2* bands; at this level, the assumption of a Gaussian probability distribution for the data is inappropriate and Poissonian statistics must be used. Thus instead of finding the best-fitting model for each source by minimizing χ^2 (χ^2 is normally used when fitting X-ray data with a higher signal-to-noise ratio and assumes Gaussian statistics), the best-fit parameters (normalization and index) were calculated by minimizing the Cash statistic (Cash 1979) which is appropriate when considering data with relatively few counts. The errors were calculated from the 90 percent confidence contours on the fit, using a method identical to that for χ^2 (see Cash 1979). A model for the total number of counts in each band, which included the model of the background, was constructed for each source and compared with the actual data (i.e. source plus background). The detector response function and corrections for vignetting effects and particle contamination were folded into the model. The results of this spectral fitting procedure have been verified by extensive simulation. A complete discussion of the X-ray spectral fitting procedure for AGN and other sources in the RIXOS survey (i.e. including AGN, emission line galaxies, clusters and stars) is presented in Mittaz et al. (1996).

The best-fitting X-ray spectral indices and their 90% (Cash) errors are given in Table 1; $\alpha_{\rm x}$, and indeed *all* spectral indices (α) are defined throughout such that $F_\nu \propto \nu^{-\alpha}$.

2.1.1 Luminosities

The logarithms of the luminosities at 0.2 keV ($L_{0.2\rm keV}$) and 2 keV ($L_{2\rm keV}$) in erg s^{-1} Hz^{-1} in the rest-frame of the quasar were calculated using the best-fit power-law model for each individual source, assuming a value of 50 km s^{-1} Mpc^{-1} for the Hubble constant (H_0) and 0 for the deceleration parameter (q_0; these values are assumed throughout this paper). Errors on the X-ray luminosities have been calculated from the Cash 90% limits on the best-fitting power-law models (including uncertainties on both the slope and normalization); $L_{0.2\rm keV}$, $L_{2\rm keV}$ and their respective errors are listed in Table 1.

2.1.2 Spurious correlations

Because the RIXOS sample is flux-limited, spurious correlations may be introduced between the various continuum parameters (slopes and luminosities) and these must be borne in mind when considering the viability of trends and relationships in the data. Sources are selected according to their flux in the hard (0.4-2.0 keV) band in the observer frame, thus 2 keV in the rest-frame of the AGN is contained within
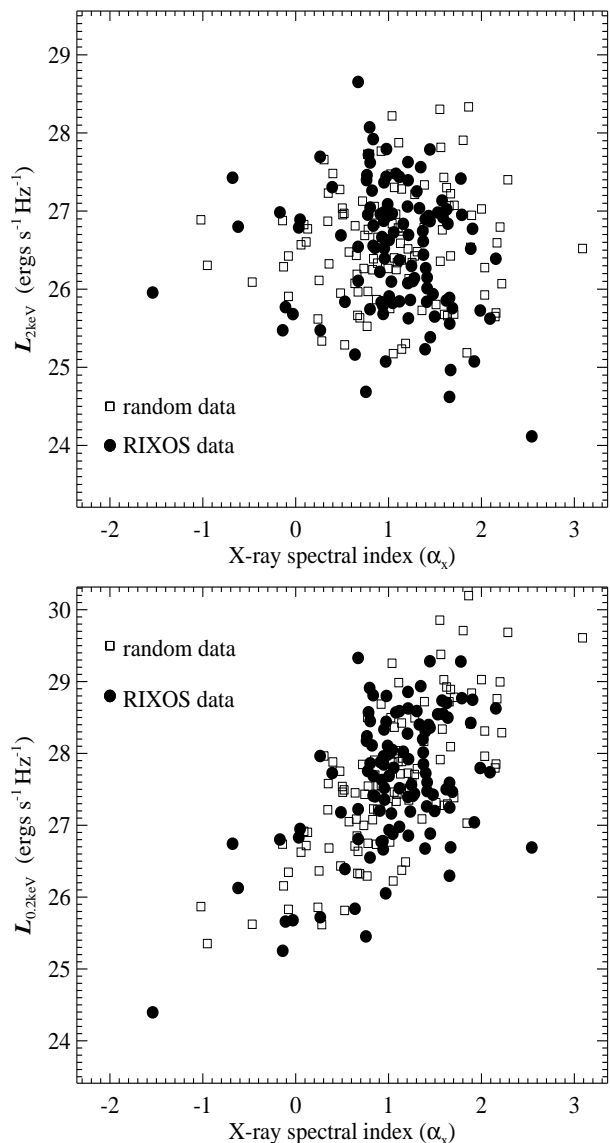

Figure 2. The X-ray luminosities at (a) 2.0 keV ($L_{2\rm keV}$) and (b) 0.2 keV ($L_{0.2\rm keV}$) plotted as a function of X-ray spectral index, $\alpha_{\rm x}$ (filled circles). Also plotted (as open squares) are comparison, random datasets (see Section 2.1.2) to illustrate the spurious correlation between $L_{0.2\rm keV}$ and $\alpha_{\rm x}$.

the observed range for all of the objects in this sample. In contrast, the rest-frame 0.2 keV flux is derived from an extrapolation of the fitted data at all but the lowest redshifts, therefore the inferred flux at 0.2 keV depends upon the X-ray slope and $L_{0.2\rm keV}$ may show an induced correlation with $\alpha_{\rm x}$.

To illustrate this problem, $L_{2\rm keV}$ and $L_{0.2\rm keV}$ are plotted as a function of $\alpha_{\rm x}$ in Fig 2. There is no apparent relationship between the $L_{2\rm keV}$ and the X-ray slope ($\alpha_{\rm x}$), but there is a strong correlation between $\alpha_{\rm x}$ and $L_{0.2\rm keV}$, i.e. when the X-ray spectrum is very soft, $L_{0.2\rm keV}$ is high and when $\alpha_{\rm x}$ is hard, $L_{0.2\rm keV}$ is low. This is consistent with the anticipated selection effect. To verify that the trends in the observed data are similar to those in a random distribution, random samples of $\alpha_{\rm x}$ and $L_{2\rm keV}$ were generated. The random data

were created by calculating the mean and standard deviations of the observed α_x and L_{2keV} and using these to generate random samples with a normal (Gaussian) probability distribution. The $L_{0.2keV}$ of this comparison sample is the sum of the random α_x and L_{2keV} (recalling that $L_{0.2keV}$ and L_{2keV} are defined here as logarithmic quantities).

The random data are compared with the observed quantities in Fig 2; both the L_{2keV} and $L_{0.2keV}$ distributions with α_x are similar in the observed and simulated datasets. This shows that the apparent correlation between α_x and $L_{0.2keV}$ is consistent with the limitations of the sample's selection criteria and may not therefore reflect a 'true' property of AGN.

The spurious dependence between $L_{0.2keV}$ and α_x might also affect relationships with $L_{0.2keV}$ and with α_{os} (the 2500 Å-to-0.2 keV ratio) and the significance of this effect is discussed where appropriate in Section 3.2. We do not expect any spurious dependences between the optical parameters (i.e. α_{opt} and L_{2500}) and L_{2keV} or α_x.

2.2 Optical data

The optical spectra were obtained over several observing runs with the Isaac Newton (INT) and William Herschel Telescopes (WHT) at the Observatorio del Roque de los Muchachos, La Palma. Two different instruments were used, the Faint Object Spectrograph (FOS) on the INT and the Intermediate-Dispersion Spectrograph and Imaging System (ISIS) on the WHT (these are indicated in Table 1). The FOS spectra cover a range of 3500Å to 10000Å with a resolution of 15-20Å FWHM in the red and 8-10Å FWHM in the blue, while ISIS spectra cover 3000Å to 9000Å with a resolution of 3Å FWHM in the red and 2Å in the blue. All spectra were taken using a narrow slit and with the slit positioned at the parallactic angle except where indicated in Table 1.

CCD images of 23 of these AGN were also obtained at the Jacobus Kapteyn (JKT) and Nordic Optical (NOT) Telescopes and these were used to check for the amount of light typically lost around the narrow slit. For these AGN, the average ratio of fluxes measured from the CCD images to fluxes measured from the optical spectra was 1.23±0.12. Objects which had a strong galactic contribution in the CCD images were not included in this calculation.

2.2.1 Optical slope

Measurements of the optical continuum slope were made by fitting a single power-law to the spectrum, having first removed all emission and absorption features. The full wavelength coverage of the spectrum was used, but ignoring regions of poor data. No correction was made for any host galaxy contamination, although we expect that this effect is small in AGN with a redshift, $z > 0.25$. It has been demonstrated that the combination of Balmer continuum emission and blended FeII lines may produce a 'quasi'-continuum that may affect the measurement of the slope of any underlying continuum (e.g. Wills, Netzer and Wills 1985). In this analysis, no correction for the Balmer continuum or FeII emission has been made unless they have formed a distinct emission feature; in this case the features were removed before fitting the overall continuum.

The best-fit observer-frame optical power-law indices (α_{opt}) are listed in Table 1. Indices were not measured from spectra not taken at the parallactic angle. Errors on the optical slopes are dominated by systematics and are difficult to determine for individual spectra. We have assessed the typical error expected on the slopes from the dispersion in the measured values for source observed more than once and estimate that the uncertainty in α_{opt} is conservatively $\sim \pm0.5$.

2.2.2 Luminosities

The logarithm of the optical continuum luminosity in the quasar rest-frame at 2500Å (L_{2500}; also given in Table 1) was calculated from the best-fitting power-law model fit to the spectra. Luminosities of sources for which CCD data were also available were explicitly corrected for any light lost around the slit; these are indicated in Table 1. Where CCD images are not available, the luminosities have been increased by the mean factor of 1.23 (see Section 2.2). For spectra not taken at the parallactic angle, luminosities were calculated from a power law spectrum which was fitted to the red part of the spectrum only (these are also indicated in Table 1). Again, errors on L_{2500} are dominated by systematics; taking into account possible variability, light losses around the slit and errors on the power-law fits, we estimate that uncertainties on optical luminosities are typically $\sim50\%$.

3 RESULTS

In the remainder of this paper, we shall include a discussion of the optical/UV BBB and the soft X-ray excess in AGN continua, thus it is important to differentiate between these. Therefore we use the term 'BBB' to refer to the rise in the optical/UV continuum towards the blue, the 'soft X-ray excess' to the excess above an extrapolation of the hard X-ray power-law at energies below ~1 keV, and the 'big bump' refers to an optical-to-soft X-ray component which incorporates the two former features.

We shall be describing much of the changes observed in the RIXOS optical and X-ray spectra in terms of the gradients of the continuum slopes. Different terminologies are commonly used in the literature for the slopes in the optical and the X-ray ranges, thus to avoid any confusion, we have adopted a single convention for both, i.e. using the terms "soft" and "hard". A "soft" slope falls towards high energies and has a relatively high energy index α (recalling here that the negative sign is implicit in our definition of α); in the optical region, a soft slope corresponds to a "red" continuum. A "hard" slope *rises* towards high energy and has a low or negative α; this corresponds to a "blue" slope in the optical. To describe changes in slope, we will use the terms "soften" (i.e. α increasing) and "harden" (where α is decreasing).

3.1 Sample properties

3.1.1 X-ray power-law slope

The average α_x for the RIXOS AGN is 1.07±0.63 (1σ standard deviation); this is harder than that of WF (1.50±0.48)

Table 1: Optical and X-ray continuum parameters.

FID	S No	Tel	z	N_{HGal}	L_{2500}	$L_{0.2\mathrm{keV}}$	$L_{2\mathrm{keV}}$	α_{opt}	α_{x}	α_{os}	α_{ox}
(1)	(2)	(3)	(4)	(5)	(6)	(7)	(8)	(9)	(10)	(11)	(12)
110	1	WHT	0.364	1.1	28.9	$27.46^{+0.03}_{-0.03}$	$25.75^{+0.05}_{-0.06}$	1.3	$1.69^{+0.06}_{-0.09}$	$0.9^{+0.2}_{-0.2}$	$1.19^{+0.09}_{-0.13}$
110	8	WHT	0.938	1.1	29.0	$27.68^{+0.10}_{-0.14}$	$26.62^{+0.06}_{-0.07}$	2.0	$1.01^{+0.11}_{-0.19}$	$0.8^{+0.3}_{-0.3}$	$0.91^{+0.08}_{-0.13}$
110	34	WHT	1.235	1.1	29.6	$26.83^{+0.25}_{-0.70}$	$26.79^{+0.08}_{-0.09}$	2.9	$0.03^{+0.46}_{-0.37}$	$1.7^{+0.6}_{-0.3}$	$1.08^{+0.07}_{-0.14}$
110	35	WHT	0.582	1.1	28.8	$27.59^{+0.06}_{-0.07}$	$25.88^{+0.08}_{-0.10}$	0.5	$1.66^{+0.11}_{-0.17}$	$0.8^{+0.2}_{-0.2}$	$1.12^{+0.07}_{-0.14}$
110	50	WHT	1.335	1.1	29.4	$27.98^{+0.11}_{-0.15}$	$26.94^{+0.06}_{-0.06}$	−0.3	$0.99^{+0.12}_{-0.19}$	$0.9^{+0.3}_{-0.3}$	$0.94^{+0.14}_{-0.13}$
122	1	WHT	1.134	4.1	30.3	$28.30^{+0.18}_{-0.33}$	$26.89^{+0.05}_{-0.06}$	0.4	$1.40^{+0.28}_{-0.22}$	$1.2^{+0.4}_{-0.3}$	$1.29^{+0.09}_{-0.13}$
122	14[45]	WHT	0.379	4.1	29.3^i	$27.50^{+0.07}_{-0.09}$	$25.85^{+0.05}_{-0.05}$	0.4	$1.62^{+0.11}_{-0.13}$	$1.1^{+0.2}_{-0.2}$	$1.30^{+0.09}_{-0.13}$
123	1	WHT	0.282	1.2	28.7^i	$27.42^{+0.02}_{-0.02}$	$25.93^{+0.04}_{-0.04}$	1.0	$1.48^{+0.05}_{-0.06}$	$0.8^{+0.2}_{-0.2}$	$1.07^{+0.10}_{-0.12}$
123	27	WHT	0.351	1.2	28.5^i	$26.66^{+0.07}_{-0.09}$	$25.68^{+0.07}_{-0.08}$	1.4	$0.94^{+0.10}_{-0.16}$	$1.2^{+0.2}_{-0.2}$	$1.09^{+0.08}_{-0.14}$
123	41	WHT	1.818	1.2	30.5^i	$28.17^{+0.14}_{-0.21}$	$27.39^{+0.05}_{-0.06}$	1.8	$0.76^{+0.17}_{-0.17}$	$1.4^{+0.3}_{-0.3}$	$1.18^{+0.09}_{-0.13}$
123	42	WHT	0.477	1.2	28.9^i	$26.88^{+0.09}_{-0.12}$	$25.82^{+0.08}_{-0.09}$	1.0	$1.05^{+0.18}_{-0.14}$	$1.3^{+0.3}_{-0.2}$	$1.17^{+0.07}_{-0.14}$
123	46	WHT	1.288	1.2	29.7^i	$26.94^{+0.24}_{-0.59}$	$26.89^{+0.07}_{-0.08}$	1.7	$0.05^{+0.36}_{-0.30}$	$1.7^{+0.6}_{-0.3}$	$1.09^{+0.08}_{-0.14}$
123	66	WHT	0.494	1.2	28.9	$27.16^{+0.08}_{-0.09}$	$26.09^{+0.06}_{-0.08}$	1.1	$1.03^{+0.10}_{-0.16}$	$1.1^{+0.2}_{-0.2}$	$1.07^{+0.08}_{-0.13}$
123	85	WHT	0.652	1.2	29.8	$28.42^{+0.03}_{-0.03}$	$26.51^{+0.05}_{-0.06}$	−0.1	$1.89^{+0.06}_{-0.10}$	$0.9^{+0.2}_{-0.2}$	$1.25^{+0.11}_{-0.11}$
126	27[36]	WHT	3.305	2.0	30.3^i	$29.32^{+0.15}_{-0.23}$	$28.65^{+0.05}_{-0.05}$	0.8	$0.67^{+0.16}_{-0.15}$	$0.7^{+0.3}_{-0.3}$	$0.67^{+0.09}_{-0.13}$
127	3	WHT	1.038	1.7	30.2	$28.76^{+0.05}_{-0.06}$	$26.95^{+0.05}_{-0.06}$	0.6	$1.79^{+0.08}_{-0.12}$	$0.9^{+0.2}_{-0.2}$	$1.26^{+0.09}_{-0.13}$
127	4	INT	0.973	1.7	30.2	$28.35^{+0.07}_{-0.09}$	$26.87^{+0.05}_{-0.06}$	0.1	$1.45^{+0.09}_{-0.15}$	$1.1^{+0.2}_{-0.2}$	$1.26^{+0.09}_{-0.13}$
127	21	WHT	0.152	1.7	27.2	$26.05^{+0.06}_{-0.08}$	$25.07^{+0.06}_{-0.07}$	np	$0.97^{+0.12}_{-0.12}$	$0.7^{+0.2}_{-0.2}$	$0.82^{+0.09}_{-0.14}$
133	22	WHT	1.788	1.2	31.1	$28.45^{+0.15}_{-0.23}$	$27.62^{+0.06}_{-0.07}$	0.5	$0.80^{+0.20}_{-0.22}$	$1.6^{+0.3}_{-0.3}$	$1.33^{+0.08}_{-0.13}$
206	6	WHT	0.690	3.7	29.7	$27.22^{+0.21}_{-0.44}$	$26.54^{+0.06}_{-0.07}$	0.6	$0.67^{+0.35}_{-0.29}$	$1.5^{+0.5}_{-0.3}$	$1.19^{+0.08}_{-0.13}$
206	9	WHT	0.801	3.7	28.9	$27.18^{+0.22}_{-0.51}$	$26.68^{+0.06}_{-0.06}$	0.7	$0.49^{+0.38}_{-0.31}$	$1.1^{+0.5}_{-0.3}$	$0.88^{+0.09}_{-0.13}$
208	2	WHT	0.387	0.7	28.8	$27.44^{+0.03}_{-0.03}$	$26.14^{+0.04}_{-0.05}$	2.0	$1.28^{+0.05}_{-0.08}$	$0.8^{+0.2}_{-0.2}$	$1.01^{+0.09}_{-0.13}$
208	55	WHT	1.718	0.7	30.1	$28.23^{+0.10}_{-0.14}$	$27.46^{+0.05}_{-0.05}$	1.6	$0.77^{+0.14}_{-0.14}$	$1.2^{+0.3}_{-0.3}$	$1.03^{+0.09}_{-0.13}$
211	30	INT	1.420	4.0	30.7	$28.33^{+0.21}_{-0.46}$	$27.36^{+0.05}_{-0.06}$	0.8	$0.95^{+0.34}_{-0.26}$	$1.4^{+0.5}_{-0.3}$	$1.26^{+0.09}_{-0.13}$
211	42	INT	0.232	4.0	28.9	$26.88^{+0.10}_{-0.13}$	$25.38^{+0.07}_{-0.09}$	1.9	$1.45^{+0.13}_{-0.21}$	$1.2^{+0.3}_{-0.3}$	$1.33^{+0.08}_{-0.14}$
212	6	WHT	1.004	1.2	29.8	$27.68^{+0.17}_{-0.29}$	$26.81^{+0.09}_{-0.11}$	0.2	$0.84^{+0.27}_{-0.25}$	$1.3^{+0.4}_{-0.3}$	$1.14^{+0.07}_{-0.14}$
212	16	WHT	0.843	1.2	30.1	$27.51^{+0.16}_{-0.27}$	$26.52^{+0.10}_{-0.13}$	0.3	$0.95^{+0.28}_{-0.26}$	$1.6^{+0.4}_{-0.3}$	$1.37^{+0.06}_{-0.15}$
212	25	WHT	0.801	1.2	29.7^i	$28.01^{+0.09}_{-0.12}$	$26.61^{+0.09}_{-0.10}$	0.2	$1.37^{+0.18}_{-0.17}$	$1.1^{+0.3}_{-0.2}$	$1.20^{+0.07}_{-0.14}$
213	17	WHT	0.438	4.4	29.0	$27.47^{+0.21}_{-0.44}$	$26.01^{+0.12}_{-0.16}$	0.3	$1.42^{+0.42}_{-0.34}$	$1.0^{+0.5}_{-0.3}$	$1.15^{+0.05}_{-0.16}$
213	19	WHT	0.467	4.4	29.0	$27.59^{+0.18}_{-0.31}$	$26.15^{+0.09}_{-0.12}$	1.1	$1.42^{+0.31}_{-0.29}$	$0.9^{+0.4}_{-0.3}$	$1.09^{+0.06}_{-0.15}$
215	1	INT	2.248	1.2	31.1	$28.80^{+0.15}_{-0.24}$	$27.79^{+0.06}_{-0.07}$	0.6	$0.98^{+0.22}_{-0.19}$	$1.4^{+0.3}_{-0.3}$	$1.27^{+0.08}_{-0.13}$
215	19	WHT	0.584	1.2	29.5	$27.85^{+0.05}_{-0.06}$	$26.44^{+0.06}_{-0.08}$	1.1	$1.38^{+0.09}_{-0.14}$	$1.0^{+0.2}_{-0.2}$	$1.18^{+0.08}_{-0.14}$
215	32	WHT	0.613	1.2	29.4	$27.39^{+0.12}_{-0.18}$	$26.07^{+0.12}_{-0.17}$	−0.1	$1.21^{+0.19}_{-0.30}$	$1.2^{+0.3}_{-0.3}$	$1.28^{+0.18}_{-0.14}$
216	7	WHT	0.804	3.5	29.5^i	$27.41^{+0.22}_{-0.49}$	$26.55^{+0.06}_{-0.08}$	−1.1	$0.84^{+0.37}_{-0.30}$	$1.3^{+0.5}_{-0.3}$	$1.12^{+0.05}_{-0.12}$
217	3	WHT	0.989	1.1	29.7^i	$27.92^{+0.08}_{-0.10}$	$26.69^{+0.06}_{-0.07}$	0.3	$1.22^{+0.13}_{-0.12}$	$1.1^{+0.2}_{-0.2}$	$1.15^{+0.08}_{-0.13}$
217	21[52]	WHT	0.562	1.1	28.6	$27.40^{+0.07}_{-0.08}$	$26.10^{+0.09}_{-0.08}$	1.5	$1.26^{+0.10}_{-0.16}$	$0.7^{+0.2}_{-0.2}$	$0.95^{+0.08}_{-0.14}$
217	34	WHT	1.200	1.1	30.3	$28.40^{+0.06}_{-0.07}$	$27.03^{+0.05}_{-0.14}$	np	$1.33^{+0.08}_{-0.12}$	$1.2^{+0.2}_{-0.2}$	$1.26^{+0.16}_{-0.17}$
217	35	WHT	0.435	1.1	28.6^i	$26.77^{+0.08}_{-0.11}$	$25.83^{+0.07}_{-0.08}$	1.8	$0.92^{+0.15}_{-0.14}$	$1.2^{+0.3}_{-0.2}$	$1.07^{+0.08}_{-0.14}$
217	59	WHT	0.587	1.1	28.6	$27.51^{+0.06}_{-0.07}$	$26.37^{+0.05}_{-0.06}$	1.6	$1.12^{+0.09}_{-0.12}$	$0.7^{+0.2}_{-0.2}$	$0.84^{+0.09}_{-0.13}$
218	1	WHT	0.545	3.0	29.5^i	$27.40^{+0.17}_{-0.28}$	$26.53^{+0.08}_{-0.09}$	−0.7	$0.85^{+0.28}_{-0.25}$	$1.3^{+0.4}_{-0.3}$	$1.15^{+0.07}_{-0.14}$
218	27	WHT	0.631	3.0	29.8	$27.80^{+0.14}_{-0.21}$	$26.72^{+0.07}_{-0.08}$	np	$1.06^{+0.22}_{-0.21}$	$1.3^{+0.3}_{-0.3}$	$1.18^{+0.08}_{-0.14}$
219	15	WHT	1.190	1.3	29.6^i	$28.55^{+0.07}_{-0.09}$	$26.91^{+0.06}_{-0.07}$	1.9	$1.59^{+0.10}_{-0.16}$	$0.6^{+0.2}_{-0.2}$	$1.01^{+0.08}_{-0.13}$
219	48	WHT	1.367	1.3	29.5	$27.96^{+0.17}_{-0.30}$	$26.98^{+0.07}_{-0.09}$	0.5	$0.95^{+0.26}_{-0.23}$	$1.0^{+0.4}_{-0.3}$	$0.98^{+0.08}_{-0.15}$
220	23	WHT	0.193	3.9	27.6^i	$25.25^{+0.14}_{-0.21}$	$25.47^{+0.14}_{-0.21}$	3.8	$-0.14^{+1.04}_{-0.75}$	$1.4^{+0.3}_{-0.3}$	$0.80^{+0.03}_{-0.16}$
220	25	WHT	0.210	3.9	28.0^i	$27.04^{+0.13}_{-0.18}$	$25.07^{+0.12}_{-0.18}$	1.3	$1.92^{+0.27}_{-0.26}$	$0.6^{+0.3}_{-0.3}$	$1.13^{+0.04}_{-0.16}$
221	16	WHT	0.184	2.9	28.4	$26.69^{+0.08}_{-0.10}$	$24.96^{+0.10}_{-0.12}$	1.4	$1.67^{+0.13}_{-0.21}$	$1.0^{+0.3}_{-0.2}$	$1.31^{+0.06}_{-0.15}$
222	20	WHT	1.068	2.4	29.7	$28.19^{+0.15}_{-0.23}$	$26.74^{+0.08}_{-0.09}$	0.6	$1.37^{+0.17}_{-0.28}$	$1.0^{+0.3}_{-0.3}$	$1.14^{+0.07}_{-0.14}$
223	17	WHT	0.288	1.8	28.7^i	$27.26^{+0.02}_{-0.03}$	$25.83^{+0.03}_{-0.03}$	2.1	$1.41^{+0.04}_{-0.07}$	$0.9^{+0.2}_{-0.2}$	$1.10^{+0.10}_{-0.12}$
225	1[52]	INT	0.488	2.2	28.9^i	$26.97^{+0.11}_{-0.15}$	$25.84^{+0.08}_{-0.10}$	1.1	$1.12^{+0.19}_{-0.18}$	$1.2^{+0.3}_{-0.3}$	$1.17^{+0.07}_{-0.14}$

Table 1 (continued): Optical and X-ray continuum parameters.

FID	S No	Tel	z	N_{HGal}	L_{2500}	$L_{0.2\mathrm{keV}}$	$L_{2\mathrm{keV}}$	α_{opt}	α_{x}	α_{os}	α_{ox}
(1)	(2)	(3)	(4)	(5)	(6)	(7)	(8)	(9)	(10)	(11)	(12)
226	41	WHT	1.315	1.2	30.1^i	$28.57^{+0.04}_{-0.04}$	$27.47^{+0.02}_{-0.02}$	np	$1.08^{+0.04}_{-0.07}$	$0.9^{+0.2}_{-0.2}$	$0.98^{+0.10}_{-0.12}$
226	$114^{(49)}$	WHT	0.113	1.2	26.8	$25.45^{+0.10}_{-0.14}$	$24.68^{+0.04}_{-0.05}$	0.6	$0.76^{+0.14}_{-0.13}$	$0.8^{+0.3}_{-0.3}$	$0.81^{+0.09}_{-0.13}$
227	19	WHT	1.861	1.8	30.5^i	$28.93^{+0.09}_{-0.11}$	$27.56^{+0.04}_{-0.04}$	1.0	$1.35^{+0.10}_{-0.13}$	$1.0^{+0.3}_{-0.2}$	$1.11^{+0.09}_{-0.13}$
227	37	WHT	1.413	1.8	30.6^i	$28.85^{+0.06}_{-0.07}$	$27.62^{+0.03}_{-0.03}$	1.4	$1.21^{+0.06}_{-0.10}$	$1.1^{+0.2}_{-0.2}$	$1.14^{+0.10}_{-0.12}$
227	301	WHT	0.114	1.8	27.6^i	$26.69^{+0.02}_{-0.02}$	$24.11^{+0.08}_{-0.09}$	1.7	$2.54^{+0.07}_{-0.12}$	$0.6^{+0.2}_{-0.2}$	$1.33^{+0.08}_{-0.14}$
227	513	WHT	0.959	1.8	30.0^i	$27.87^{+0.07}_{-0.09}$	$26.96^{+0.04}_{-0.04}$	−0.1	$0.91^{+0.10}_{-0.10}$	$1.3^{+0.2}_{-0.2}$	$1.17^{+0.10}_{-0.12}$
228	1	INT	1.726	3.7	30.8	$27.96^{+0.26}_{-0.77}$	$27.69^{+0.07}_{-0.09}$	0.4	$0.26^{+0.40}_{-0.35}$	$1.8^{+0.7}_{-0.4}$	$1.18^{+0.08}_{-0.14}$
231	301	WHT	0.783	0.7	30.2	$28.49^{+0.04}_{-0.04}$	$26.83^{+0.10}_{-0.12}$	0.5	$1.64^{+0.08}_{-0.10}$	$1.0^{+0.2}_{-0.2}$	$1.27^{+0.11}_{-0.11}$
231	302	INT	1.572	0.7	30.5	$28.58^{+0.08}_{-0.10}$	$27.43^{+0.05}_{-0.06}$	0.6	$1.12^{+0.12}_{-0.14}$	$1.2^{+0.3}_{-0.2}$	$1.19^{+0.09}_{-0.13}$
231	503	INT	0.234	0.7	28.3	$25.66^{+0.09}_{-0.12}$	$25.77^{+0.06}_{-0.08}$	2.1	$-0.11^{+0.15}_{-0.13}$	$1.7^{+0.3}_{-0.2}$	$0.97^{+0.08}_{-0.13}$
232	16	WHT	0.227	0.8	28.3	$25.83^{+0.14}_{-0.22}$	$25.16^{+0.11}_{-0.15}$	2.2	$0.64^{+0.28}_{-0.24}$	$1.5^{+0.3}_{-0.3}$	$1.20^{+0.05}_{-0.15}$
232	301	INT	0.385	0.8	29.3	$26.77^{+0.07}_{-0.09}$	$25.78^{+0.08}_{-0.10}$	0.6	$0.94^{+0.11}_{-0.18}$	$1.6^{+0.2}_{-0.2}$	$1.35^{+0.07}_{-0.14}$
234	1	INT	1.666	4.1	30.7	$29.28^{+0.13}_{-0.20}$	$27.78^{+0.04}_{-0.05}$	1.0	$1.45^{+0.13}_{-0.21}$	$0.9^{+0.3}_{-0.3}$	$1.12^{+0.09}_{-0.13}$
234	33	WHT	1.019	4.1	29.8	$28.74^{+0.13}_{-0.19}$	$26.77^{+0.07}_{-0.08}$	0.1	$1.90^{+0.16}_{-0.26}$	$0.6^{+0.3}_{-0.3}$	$1.15^{+0.08}_{-0.14}$
240	15	WHT	1.263	1.2	29.7	$28.39^{+0.05}_{-0.06}$	$26.93^{+0.04}_{-0.04}$	0.5	$1.43^{+0.067}_{-0.11}$	$0.8^{+0.2}_{-0.2}$	$1.07^{+0.09}_{-0.13}$
240	82	WHT	0.518	1.2	29.4	$26.80^{+0.07}_{-0.09}$	$26.10^{+0.04}_{-0.05}$	−0.1	$0.67^{+0.08}_{-0.13}$	$1.6^{+0.2}_{-0.2}$	$1.25^{+0.09}_{-0.13}$
248	2	INT	0.274	1.5	27.7	$26.55^{+0.06}_{-0.07}$	$25.74^{+0.05}_{-0.06}$	2.4	$0.80^{+0.11}_{-0.11}$	$0.7^{+0.2}_{-0.2}$	$0.75^{+0.09}_{-0.13}$
252	9	WHT	0.673	0.8	29.3^i	$27.56^{+0.07}_{-0.09}$	$26.29^{+0.08}_{-0.10}$	−0.3	$1.25^{+0.15}_{-0.14}$	$1.1^{+0.2}_{-0.2}$	$1.15^{+0.07}_{-0.14}$
252	34	WHT	0.680	0.8	28.9	$27.20^{+0.11}_{-0.15}$	$26.22^{+0.09}_{-0.11}$	0.5	$0.91^{+0.14}_{-0.24}$	$1.0^{+0.3}_{-0.3}$	$1.00^{+0.07}_{-0.14}$
252	36	WHT	1.037	0.8	29.3	$28.04^{+0.07}_{-0.09}$	$26.96^{+0.06}_{-0.07}$	0.7	$1.04^{+0.09}_{-0.15}$	$0.8^{+0.2}_{-0.2}$	$0.90^{+0.08}_{-0.13}$
252	38	WHT	0.216	0.8	28.7	$26.85^{+0.03}_{-0.03}$	$25.62^{+0.05}_{-0.06}$	0.6	$1.21^{+0.07}_{-0.09}$	$1.1^{+0.2}_{-0.2}$	$1.17^{+0.09}_{-0.13}$
253	5	WHT	1.211	1.6	29.6	$28.02^{+0.13}_{-0.20}$	$26.83^{+0.07}_{-0.09}$	0.5	$1.16^{+0.21}_{-0.19}$	$1.0^{+0.3}_{-0.3}$	$1.04^{+0.08}_{-0.14}$
253	32	WHT	0.237	1.6	28.5	$26.67^{+0.07}_{-0.09}$	$25.23^{+0.09}_{-0.12}$	0.2	$1.39^{+0.12}_{-0.19}$	$1.1^{+0.2}_{-0.2}$	$1.24^{+0.07}_{-0.15}$
254	10	INT	0.936	1.1	31.1	$28.73^{+0.04}_{-0.05}$	$27.13^{+0.05}_{-0.05}$	0.6	$1.58^{+0.07}_{-0.11}$	$1.5^{+0.2}_{-0.2}$	$1.53^{+0.09}_{-0.13}$
254	11	INT	1.166	1.1	30.9	$28.59^{+0.07}_{-0.08}$	$27.25^{+0.05}_{-0.06}$	0.7	$1.30^{+0.09}_{-0.14}$	$1.4^{+0.2}_{-0.2}$	$1.39^{+0.09}_{-0.13}$
254	41	WHT	0.486	1.1	29.2	$27.19^{+0.11}_{-0.14}$	$25.86^{+0.11}_{-0.15}$	0.3	$1.23^{+0.17}_{-0.27}$	$1.3^{+0.3}_{-0.3}$	$1.28^{+0.05}_{-0.15}$
255	19	WHT	0.862	5.1	29.6	$28.62^{+0.21}_{-0.46}$	$26.39^{+0.12}_{-0.17}$	0.6	$2.16^{+0.41}_{-0.38}$	$0.6^{+0.5}_{-0.3}$	$1.23^{+0.04}_{-0.16}$
257	$1^{(53)}$	INT	1.021	2.2	30.8	$28.62^{+0.06}_{-0.07}$	$27.39^{+0.04}_{-0.04}$	0.2	$1.21^{+0.07}_{-0.11}$	$1.3^{+0.2}_{-0.2}$	$1.30^{+0.10}_{-0.12}$
257	14	WHT	1.096	2.2	28.6	$27.75^{+0.17}_{-0.31}$	$26.95^{+0.06}_{-0.08}$	1.0	$0.78^{+0.25}_{-0.24}$	$0.5^{+0.4}_{-0.3}$	$0.62^{+0.08}_{-0.13}$
257	20	INT	1.304	2.2	30.2	$28.01^{+0.20}_{-0.39}$	$26.95^{+0.08}_{-0.10}$	0.3	$1.02^{+0.29}_{-0.30}$	$1.4^{+0.4}_{-0.3}$	$1.25^{+0.07}_{-0.14}$
257	38	INT	1.260	2.2	30.6	$28.10^{+0.18}_{-0.34}$	$27.08^{+0.07}_{-0.09}$	0.0	$0.99^{+0.27}_{-0.26}$	$1.6^{+0.4}_{-0.3}$	$1.34^{+0.08}_{-0.14}$
258	1	WHT	0.698	3.4	28.1	$26.80^{+0.18}_{-0.34}$	$26.98^{+0.04}_{-0.04}$	2.4	$-0.17^{+0.27}_{-0.26}$	$0.8^{+0.4}_{-0.3}$	$0.41^{+0.09}_{-0.12}$
258	32	WHT	1.618	3.4	30.0	$28.11^{+0.27}_{-0.93}$	$27.26^{+0.08}_{-0.10}$	0.7	$0.82^{+0.49}_{-0.36}$	$1.2^{+0.8}_{-0.4}$	$1.03^{+0.07}_{-0.14}$
259	5	WHT	0.977	2.0	29.6	$27.84^{+0.14}_{-0.20}$	$26.87^{+0.06}_{-0.07}$	0.4	$0.95^{+0.19}_{-0.20}$	$1.1^{+0.3}_{-0.3}$	$1.05^{+0.08}_{-0.13}$
259	$7^{(52)}$	WHT	0.408	2.0	28.6	$26.39^{+0.21}_{-0.44}$	$25.83^{+0.09}_{-0.12}$	1.5	$0.53^{+0.40}_{-0.30}$	$1.4^{+0.5}_{-0.3}$	$1.07^{+0.06}_{-0.15}$
259	$11^{(37)}$	WHT	0.995	2.0	29.3	$27.63^{+0.18}_{-0.33}$	$26.66^{+0.08}_{-0.11}$	0.2	$0.93^{+0.27}_{-0.28}$	$1.0^{+0.4}_{-0.3}$	$1.00^{+0.07}_{-0.14}$
260	8	INT	1.823	0.9	31.1	$28.44^{+0.13}_{-0.19}$	$27.43^{+0.06}_{-0.08}$	1.3	$0.97^{+0.18}_{-0.19}$	$1.7^{+0.3}_{-0.3}$	$1.41^{+0.08}_{-0.13}$
260	44	WHT	1.504	0.9	30.2	$27.72^{+0.21}_{-0.42}$	$27.30^{+0.07}_{-0.08}$	1.4	$0.39^{+0.30}_{-0.25}$	$1.5^{+0.5}_{-0.3}$	$1.09^{+0.08}_{-0.14}$
265	1	WHT	2.336	1.1	31.7	$28.91^{+0.11}_{-0.15}$	$28.07^{+0.04}_{-0.04}$	1.5	$0.80^{+0.10}_{-0.16}$	$1.8^{+0.3}_{-0.3}$	$1.40^{+0.09}_{-0.13}$
265	17	WHT	0.448	1.1	29.0	$26.93^{+0.09}_{-0.11}$	$25.90^{+0.08}_{-0.10}$	0.4	$1.01^{+0.16}_{-0.16}$	$1.3^{+0.3}_{-0.2}$	$1.16^{+0.07}_{-0.14}$
266	32	INT	2.460	2.1	31.0	$28.57^{+0.16}_{-0.27}$	$27.72^{+0.20}_{-0.39}$	0.8	$0.78^{+0.98}_{-0.57}$	$1.5^{+0.4}_{-0.3}$	$1.25^{+-0.0}_{-0.19}$
268	11	WHT	1.196	2.1	28.9	$26.12^{+0.15}_{-0.23}$	$26.80^{+0.24}_{-0.10}$	1.2	$-0.62^{+0.85}_{-0.68}$	$1.7^{+0.3}_{-0.3}$	$0.78^{+0.11}_{-0.11}$
268	24	INT	0.251	2.1	29.2	$27.73^{+0.03}_{-0.03}$	$25.62^{+0.06}_{-0.07}$	1.4	$2.09^{+0.06}_{-0.10}$	$0.9^{+0.2}_{-0.2}$	$1.35^{+0.08}_{-0.13}$
271	2	INT	0.446	2.1	29.0	$27.79^{+0.08}_{-0.10}$	$25.72^{+0.12}_{-0.17}$	1.6	$1.99^{+0.16}_{-0.25}$	$0.8^{+0.3}_{-0.2}$	$1.26^{+0.04}_{-0.16}$
271	7	WHT	1.039	2.1	30.0	$28.70^{+0.10}_{-0.14}$	$27.02^{+0.08}_{-0.10}$	0.4	$1.63^{+0.16}_{-0.20}$	$0.8^{+0.3}_{-0.3}$	$1.12^{+0.07}_{-0.14}$
272	23	INT	0.095	4.7	27.6	$26.29^{+0.11}_{-0.15}$	$24.62^{+0.09}_{-0.12}$	2.8	$1.65^{+0.20}_{-0.21}$	$0.8^{+0.3}_{-0.3}$	$1.15^{+0.06}_{-0.15}$
273	4	INT	1.046	2.8	30.5	$28.54^{+0.15}_{-0.23}$	$26.98^{+0.09}_{-0.11}$	0.7	$1.53^{+0.25}_{-0.23}$	$1.2^{+0.3}_{-0.3}$	$1.33^{+0.07}_{-0.14}$
273	6	INT	0.270	2.8	29.4	$27.35^{+0.06}_{-0.08}$	$26.39^{+0.05}_{-0.05}$	1.0	$0.96^{+0.11}_{-0.11}$	$1.3^{+0.2}_{-0.2}$	$1.16^{+0.09}_{-0.13}$
273	18	WHT	0.361	2.8	28.7	$27.19^{+0.15}_{-0.24}$	$25.64^{+0.14}_{-0.20}$	0.8	$1.50^{+0.31}_{-0.28}$	$0.9^{+0.3}_{-0.3}$	$1.15^{+0.03}_{-0.16}$

Table 1 (continued): Optical and X-ray continuum parameters.

FID	S No	Tel	z	N_{HGal}	L_{2500}	$L_{0.2\mathrm{keV}}$	$L_{2\mathrm{keV}}$	α_{opt}	α_{x}	α_{os}	α_{ox}
(1)	(2)	(3)	(4)	(5)	(6)	(7)	(8)	(9)	(10)	(11)	(12)
274	8	INT	0.156	2.1	29.2	$27.24^{+0.04}_{-0.04}$	$25.55^{+0.06}_{-0.07}$	1.1	$1.66^{+0.07}_{-0.12}$	$1.2^{+0.2}_{-0.2}$	$1.40^{+0.08}_{-0.13}$
277	1	WHT	0.595	1.7	29.8	$27.72^{+0.09}_{-0.11}$	$26.26^{+0.08}_{-0.10}$	0.2	$1.40^{+0.12}_{-0.20}$	$1.3^{+0.3}_{-0.2}$	$1.33^{+0.07}_{-0.14}$
278	9	INT	0.949	1.9	30.5	$27.86^{+0.13}_{-0.19}$	$27.04^{+0.06}_{-0.06}$	−0.1	$0.80^{+0.19}_{-0.18}$	$1.6^{+0.3}_{-0.3}$	$1.32^{+0.09}_{-0.13}$
278	10	INT	0.090	1.9	28.5	$24.39^{+0.18}_{-0.32}$	$25.95^{+0.05}_{-0.06}$	3.0	$-1.54^{+0.29}_{-0.29}$	$2.5^{+0.4}_{-0.3}$	$0.96^{+0.09}_{-0.13}$
283	6	INT	1.219	0.5	30.5	$26.74^{+0.20}_{-0.39}$	$27.42^{+0.05}_{-0.06}$	1.0	$-0.68^{+0.27}_{-0.24}$	$2.4^{+0.4}_{-0.3}$	$1.18^{+0.09}_{-0.13}$
283	14	INT	0.284	0.5	29.0	$25.67^{+0.20}_{-0.39}$	$25.68^{+0.11}_{-0.15}$	2.0	$-0.03^{+0.36}_{-0.31}$	$2.0^{+0.4}_{-0.3}$	$1.25^{+0.05}_{-0.15}$
286	2	INT	1.498	2.3	31.0	$29.27^{+0.12}_{-0.18}$	$27.41^{+0.08}_{-0.09}$	0.5	$1.78^{+0.16}_{-0.25}$	$1.1^{+0.3}_{-0.3}$	$1.38^{+0.07}_{-0.14}$
290	21$^{(43)}$	INT	2.575	1.5	31.1	$28.81^{+0.25}_{-0.65}$	$27.92^{+0.10}_{-0.12}$	0.6	$0.83^{+0.38}_{-0.31}$	$1.4^{+0.6}_{-0.3}$	$1.20^{+0.06}_{-0.15}$
293	10	WHT	0.760	4.6	29.7	$28.27^{+0.16}_{-0.26}$	$27.05^{+0.05}_{-0.06}$	0.4	$1.20^{+0.24}_{-0.22}$	$0.9^{+0.4}_{-0.3}$	$1.03^{+0.09}_{-0.13}$
293	13	WHT	0.189	4.6	27.4	$25.72^{+0.27}_{-0.95}$	$25.47^{+0.12}_{-0.16}$	2.6	$0.27^{+0.69}_{-0.60}$	$1.0^{+0.8}_{-0.4}$	$0.73^{+0.05}_{-0.16}$

(1) RIXOS field number (see Mason et al 1996); *(2)* RIXOS source number (Mason et al 1996) - the number in brackets is the radius of the extraction circle used for the X-ray data (in arcseconds) where it is less than 54 arcsec (see Section 2.1); *(3)* the telescope at which the spectrum was taken - see Section 2.2; *(4)* redshift; *(5)* Galactic column density (10^{20} cm^{-2}) - errors are ∼10 per cent (see also Section 4.2.1); *(6)* log of the monochromatic optical luminosity at 2500 Å (erg s^{-1} Hz^{-1}) - error is estimated to be ∼50 percent (Section 2.2.2); *(7)* log of the monochromatic X-ray luminosity at 0.2 keV (erg s^{-1} Hz^{-1}) - errors are calculated from the 90% errors on the fits (Section 2.1.1); *(8)* log of the monochromatic X-ray luminosity at 2.0 keV (erg s^{-1} Hz^{-1}) - errors are calculated from the 90% errors on the fits (Section 2.1.1); *(9)* energy index of the best-fitting power-law to the optical continuum - error is estimated to be ±0.5 (Section 2.2.1); *(10)* energy index of the best-fitting power-law to the X-ray data - errors are 90% (Section 2.1); *(11)* and *(12)* for definitions see Section 3.2.3 - errors are calculated from the quoted errors on L_{2500}, $L_{0.2\mathrm{keV}}$ and $L_{2\mathrm{keV}}$; ^{i} - CCD image taken; np - spectrum not taken at the parallactic angle.
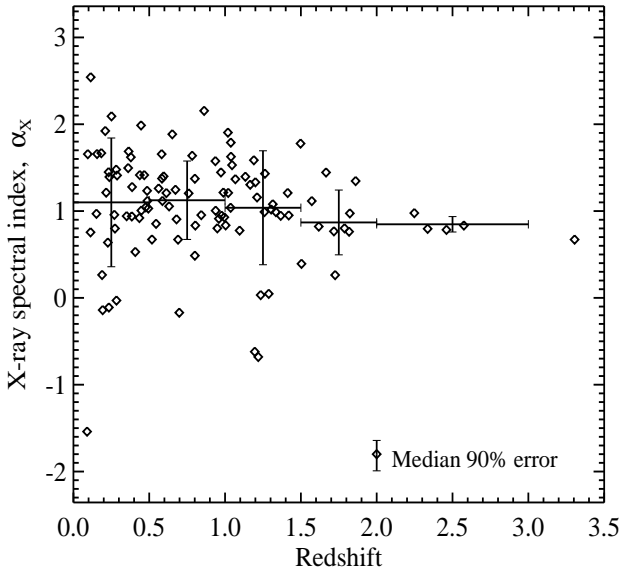

Figure 3. The X-ray spectral index, α_{x}, plotted as a function of redshift.

and suggests that the WF sample has a bias towards AGN with strong soft X-ray excesses and thus perhaps also strong BBBs. The RIXOS mean α_{x} is also harder than for the L94 sample of optically-selected quasars (1.50±0.40).

We find no significant dependence of α_{x} on redshift for this sample of the RIXOS AGN (see Fig 3), neither is there any such dependence in the complete sample (Mittaz et al. 1996). However the scatter in α_{x} may lessen at high redshifts, e.g. for $2 < z < 3$, the mean α_{x}=0.85±0.09 (standard deviation), which is similar to the mean slope of

α_{x}=0.89±0.25 measured at higher energies in low-z AGN by Comastri et al. (1992). This would be consistent with two competing trends, *1.* a tendency for the soft X-ray excess to be shifted out of the observed range as the redshift increases, and *2.* a reduced sensitivity to absorption in the rest-frame at higher redshifts, as the most strongly affected regions (at energies below ∼ 0.5keV) also move out of range.

3.1.2   Optical continuum slope

The best-fitting optical power-law slopes have been calculated over the full range of the *observed* spectra and therefore correspond to different rest-frame wavelength ranges at different redshifts. This must be taken into account when considering α_{opt}, as previous studies have shown that the optical/UV continua of individual AGN soften towards the UV (e.g. Kinney et al. 1987; O'Brien, Gondhalekar & Wilson 1988; Zheng & Malkan 1993), thus we might expect the RIXOS α_{opt} distribution to show a general softening with redshift. The optical indices are plotted in Fig 4 as a function of z, but at $z > 0.25$ (where galactic contamination is small), there are no changes with redshift within 1σ. This appears to be contrary to the previous studies mentioned, but requires further investigation with spectrophotometric optical-to-UV coverage in the rest-frame to assess its significance.

The mean α_{opt} for the RIXOS AGN is 0.92±0.76 (1σ standard deviation). This is softer than the mean slope measured for samples of optically-selected quasars, e.g. Neugebauer et al. (1987) found a median α_{opt} of 0.2 while Francis et al. (1991) measured a median index of 0.3. This suggests that the optically-selected samples may be biased towards objects with relatively strong optical/UV BBBs.
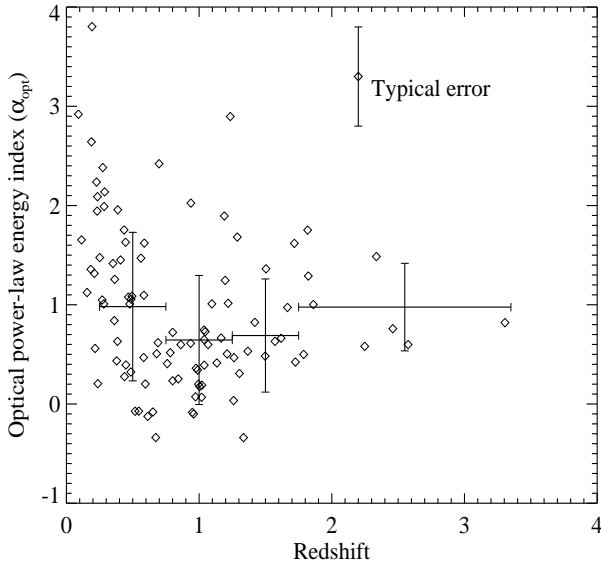
Figure 4. The slope of the best-fitting power law to the optical continuum, $\alpha_{\rm opt}$, plotted as a function of redshift.

3.1.3 Ratio of optical to X-ray fluxes

The ratios of optical (i.e. 2500 Å) to X-ray flux at 2.0 keV and 0.2 keV are parameterized using $\alpha_{\rm ox}$ (Tananbaum et al. 1979) and $\alpha_{\rm os}$ (Puchnarewicz et al. 1992) respectively. The $\alpha_{\rm ox}$ and $\alpha_{\rm os}$ are plotted as a function of redshift in Fig 5 (and listed in Table 1) and show no significant changes with z (although there is the suggestion of a possible increase in $\alpha_{\rm os}$ at $z > 1.5$).

The mean $\alpha_{\rm ox}$ for the RIXOS AGN is 1.14±0.18 (1σ standard deviation). This is lower than for optically-selected objects, e.g. for the complete sample of PG quasars,

the mean $\alpha_{\rm ox}$ is 1.50 with a range of 1.0 to 2.0 (Wilkes et al. 1994). It is also lower than the mean which we calculate for the WF sample of X-ray-bright AGN, i.e. 1.37±0.23 (1σ standard deviation). Note that the values of $\alpha_{\rm ox}$ for WF have slightly different definitions to those used for the RIXOS objects because WF measure the optical continuum flux at 2675 Å. For WF, we have calculated the optical-to-X-ray ratio using $\alpha_{\rm ox}(2675$ Å$)=(L_{2675A}-L_{2keV})/2.635$ (where L_{2675A} is the logarithm of the rest-frame luminosity at 2675 Å). By calculating the $\alpha_{\rm ox}(2675$ Å$)$ for the RIXOS AGN, we estimate that the mean difference between the two definitions of $\alpha_{\rm ox}$ [i.e. $\alpha_{\rm ox}$-$\alpha_{\rm ox}(2675$ Å$)$] is +0.02. When taking into account the difference in the definitions, we find that the 'corrected' WF mean would be 1.39±0.23, increasing the discrepancy between the samples.

The mean 2500 Å-to-*0.2* keV ratio ($\alpha_{\rm os}$) is 1.17±0.37 (1σ); however, note that this value may be biased by the selection effect inherent in $L_{0.2\rm keV}$ (see Section 2.1.2).

3.2 Correlations

All correlations in this section have been evaluated using the Spearman rank-order correlation coefficient which is a non-parametric method insensitive to outlying points. The 'correlation probabilities' given in the following sections, $p_{\rm corr}$, are expressed as percentages and are equal to 100% minus the percentage probability of being drawn from a random sample. The correlation probabilities are given for all continuum parameters in Table 2.

One problem in searching for correlations in flux-limited samples of this kind, is that luminosities are dominated by the correction for the distance to the quasar, so that the continua of low-redshift objects have low luminosities while high-z objects tend to have high luminosities. This usually results in very strong correlations between luminosities in different bands and may not reflect a real dependence. In
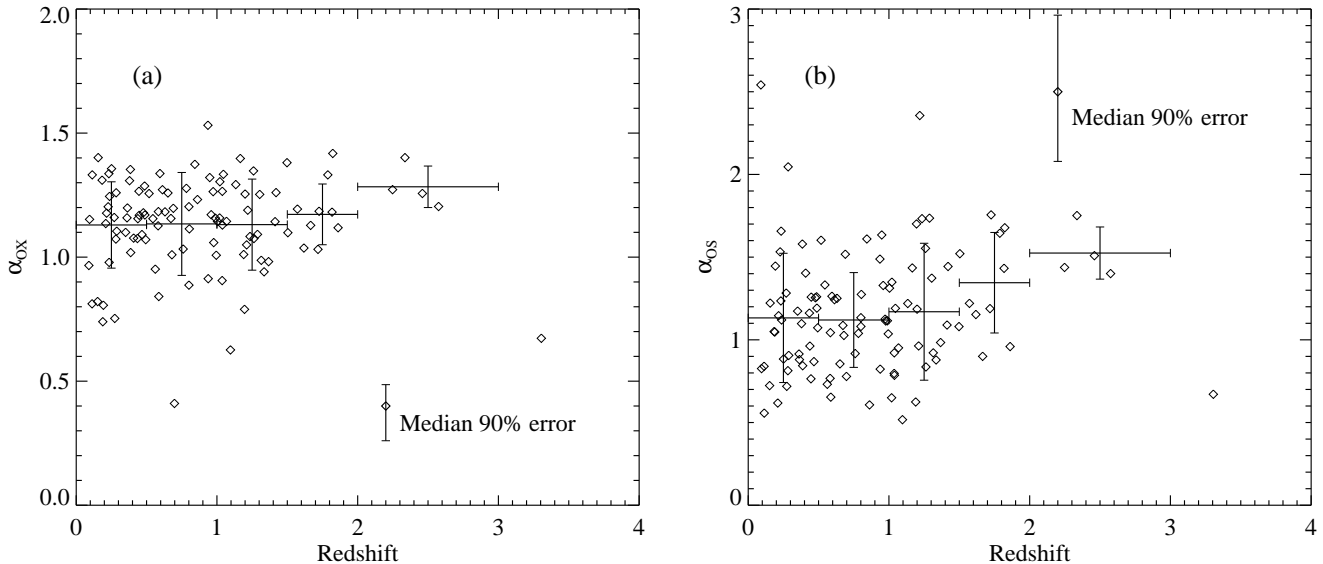

Figure 5. The ratios of optical-to-X-ray luminosity at 2.0 keV and 0.2 keV, (a) $\alpha_{\rm ox}$ and (b) $\alpha_{\rm os}$ respectively, plotted as a function of redshift. Also shown are the mean indices in intervals of $\Delta z = 0.5$ for $0 < z < 2$ and the mean for $2 < z < 3$; vertical error bars represent the standard deviation (σ) on the means.

Table 2: Continuum correlation probabilities (p_{corr}; percent)

	z (r_S) %	L_{2500} (r_S) %	$L_{0.2\mathrm{keV}}$ (r_S) %	$L_{2\mathrm{keV}}$ (r_S) %	α_{opt} (r_S) %	α_{x} (r_S) %	α_{os} (r_S) %
L_{2500}	(0.8) >99						
$L_{0.2\mathrm{keV}}$	(0.8) >99	(0.4) >99					
$L_{2\mathrm{keV}}$	(0.9) >99	(0.5) >99	(0.4) >99				
α_{opt}	(−0.3) 93	(−0.4) >99	(−0.4) >99	(−0.3) 92			
α_{x}	(−0.2) 37	(0.0) 4	(0.3) 99	(−0.2) 52	(−0.2) 68		
α_{os}	(0.2) 55	(0.4) >99	(−0.1) 2	(0.2) 75	(0.0) 4	(−0.6) >99	
α_{ox}	(0.1) 3	(0.5) >99	(0.3) 95	(0.1) 3	(−0.3) 97	(0.4) >99	(0.4) >99

The correlation coefficients between two different luminosities were calculated after having adjusted for redshift (see Section 4).

order to allow for this, when comparing parameters which are both luminosities, each pair of parameters is divided by a normalizing factor which has the redshift dependence built into it. The factor used is the rest-frame luminosity equivalent to an observed flux of 1×10^{-15} erg cm^{-2} s^{-1} (arbitrarily chosen to match the observed-flux typically measured in the optical emission lines). In Table 2, correlation probabilities have been calculated after dividing the luminosities by this factor.

3.2.1 Luminosity and X-ray slope

We find no relationship between the X-ray spectral slope and the luminosity at 2 keV; the apparent correlation between α_{x} and $L_{0.2\mathrm{keV}}$ is due to a selection effect (see Section 2.1.2). There is no correlation between α_{x} and the optical luminosity at 2500 Å.

3.2.2 Luminosity and optical slope

Table 2 shows that the slope of the optical continuum is strongly anti-correlated with L_{2500}, i.e. as the 2500 Å luminosity increases, α_{opt} becomes harder. This could be a consequence of measuring L_{2500} from optical power-law slopes which are measured in the observer's frame; the rest-frame flux at 2500 Å does not fall within the observed wavelength range below $z=0.4$ and must be extrapolated from the power-law fit at longer wavelengths. L_{2500} would then be high when α_{opt} was hard which might influence the correlation. It may also be due to contamination by the host galaxy which would have the effect of softening α_{opt} when the nuclear emission (and therefore L_{2500}) is low, indeed, Wilkes et al. (1994) found that starlight contamination was an important factor for AGN with an L_{2500} lower than $\sim$29. However at $z=0.4$, the rest-frame wavelength range over which α_{opt} is calculated lies at $\sim$2500-6400 Å where galactic contamination is already relatively low and should have only a small effect (if any) on the measurement of the optical slope.

Thus to eliminate these effects, we have excluded the $z \leq 0.4$ objects and find that while the anti-correlation does disappear for $z > 1.0$ ($r_{\mathrm{S}}=-0.1$; $p_{\mathrm{corr}}=2\%$), it remains strong at $0.4 < z < 1.0$ ($r_{\mathrm{S}}=-0.6$ and $p_{\mathrm{corr}}=99.98\%$; see also Fig 6). A similar effect is seen in the correlations between α_{opt} and $L_{0.2\mathrm{keV}}$ and between α_{opt} and $L_{2\mathrm{keV}}$ (i.e. the data are correlated for $0.4 < z < 1.0$, but not at $z > 1.0$), although the latter dependences may be induced by strong correlations between L_{2500}, $L_{0.2\mathrm{keV}}$ and $L_{2\mathrm{keV}}$ (see Table 2).
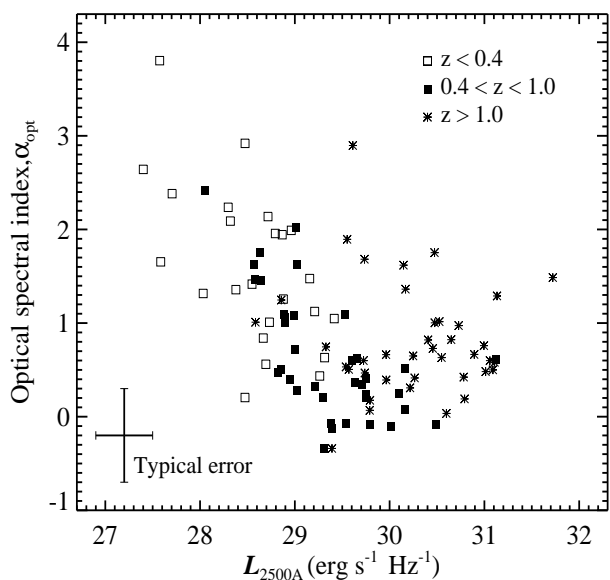

Figure 6. The optical spectral index, α_{opt}, plotted as a function of optical luminosity at 2500 Å, L_{2500}. The AGN are plotted according to their redshift, i.e. AGN with $z < 0.4$ are plotted as open squares, $0.4 < z < 1.0$ are plotted as solid squares and $z > 1.0$ as asterisks.

This might be a luminosity, rather than a wavelength-dependent effect, but it is difficult to distinguish between these due to the strong redshift dependence in the luminosities. Nonetheless, the correlations imply that at relatively low bolometric luminosity, the $\lambda > 5000$ Å region hardens as the luminosity increases, while at higher bolometric luminosities, the continuum slope at shorter wavelengths ($\lambda < 5000$ Å) is independent of luminosity. A similar effect was reported by Zheng & Malkan (1993), who found that the rest-frame 6500-3100 Å continua of their quasars and Seyfert 1s also harden significantly with luminosity ($\Delta\alpha=1.1$) while at shorter wavelengths (3100-1250 Å in the rest-frame), the change in slope is smaller over the same luminosity range ($\Delta\alpha=0.5$). To explain this, they suggest that either (1) the BBB shifts from the UV into the optical as the luminosity increases, or (2) that the BBBs are stronger in high-luminosity AGN.

3.2.3 Optical-to-X-ray luminosity ratios

We find evidence for a strong correlation between α_{ox} and α_{x} ($p_{\mathrm{corr}}=99.8\%$; see Fig 7). The 2500 Å luminosity is mea-

sured independently of the X-ray parameters and L_{2keV} is not correlated with α_x, thus we conclude that this is *not* due to any selection effects. Similar correlations have also been reported by WF and L94. This relationship suggests that when the 2500 Å-to-2 keV ratio is high, the 0.2-2 keV slope is relatively soft so that it rises steeply towards the EUV, and the overall 2500 Å-to-2 keV continuum is convex. Conversely, when α_{ox} is low, α_x is hard (i.e. it falls towards the EUV) and the 2500 Å-to-2 keV continuum is concave. Assuming that α_{ox} is an indicator of the strength of the BBB (because the BBB is strong at 2500 Å but negligible at 2 keV) and that α_x measures the strength of the soft X-ray excess, then this implies that the optical/UV BBB and the soft excess may be part of the same component.

It is important to be mindful of possible selection effects when considering such correlations, particularly in the X-ray data where the spectral resolution is low, and the response of the detector favours particular energies within the nominal bandpass. For example, Ulrich & Molendi (1996) have cautioned that the 2 keV flux inferred from ROSAT spectra is coupled to the spectral slope. They suggest that this may induce the correlations seen by WF and L94 because 2 keV, the reference energy for α_{ox}, is far removed from the centroid energy of the counts detected by the ROSAT PSPC for a typical low-redshift Seyfert, which is ∼0.4 keV for a slope, α_x∼1.6. However, there are a number of reasons why this effect is unlikely to induce the correlations seen in the RIXOS AGN. Firstly, the typical error bars, which reflect the coupling between spectral normalization and slope in the size of the uncertainty in α_{ox}, are significantly smaller than the observed range of the correlation. Secondly, the X-ray spectra of objects in our sample are typically harder than those in WF and L94 and cover a wider range in α_x; both of these factors will reduce the Ulrich & Molendi effect. Thirdly, the RIXOS AGN extend to much higher redshifts than WF and L94 moving the equivalent of the 2 keV flux in the quasar's rest-frame closer to and below the centroid energy of the photons registered in the detector frame, yet the correlation is still seen in the sample of RIXOS objects above z=1 (see Fig 7).

We also find evidence of a correlation between $L_{0.2keV}$ and α_{ox} (p_{corr}=95%), i.e. when the optical-to-X-ray ratio is high, the luminosity at 0.2 keV is also high, although this may be an induced correlation as both $L_{0.2keV}$ and α_{ox} are also correlated with α_x (and the $L_{0.2keV}$-α_x correlation is due to a selection effect; see Section 2.1.2).

Table 2 also indicates a correlation between L_{2500} and α_{ox}, but this is expected since the L_{2keV} distribution is random with α_x (Section 4.2.1) and L_{2500} is closely related to α_{ox} (i.e. L_{2500}=2.605α_{ox}+L_{2keV}). However, significant dependences have been reported elsewhere between luminosity and α_{ox} (e.g. Reichert et al. 1982; Avni & Tananbaum 1986; Wilkes et al. 1994). The correlation between L_{2500} and α_{os} is consistent with the selection effect discussed in Section 2.1.2.

3.2.4   *Optical and X-ray slopes*

There is an anti-correlation between α_{opt} and α_{ox}, implying that when the 2500 Å-to-2 keV ratio is high, the optical slope is relatively hard. There is also a weak (p_{corr}=68 per cent) anti-correlation between the optical and X-ray slopes
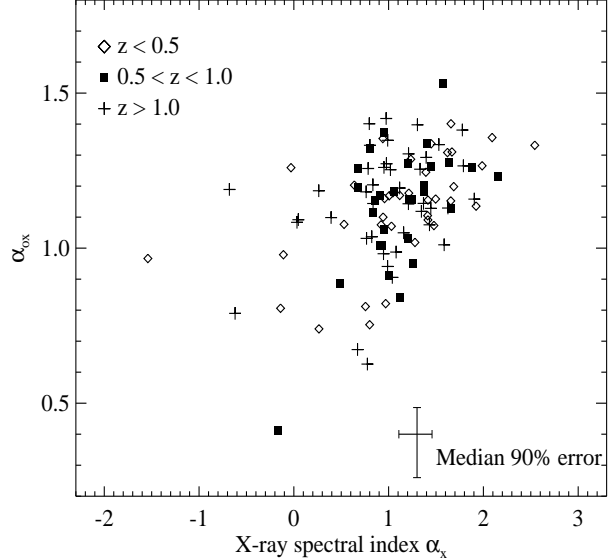

Figure 7. The optical-to-X-ray ratio, α_{ox}, plotted as a function of X-ray spectral index, α_x. The data are plotted according to the redshift of the AGN, i.e. $z < 0.5$ are plotted as diamonds, $0.5 < z < 1.0$ are plotted as filled boxes and $z > 1.0$ as crosses.
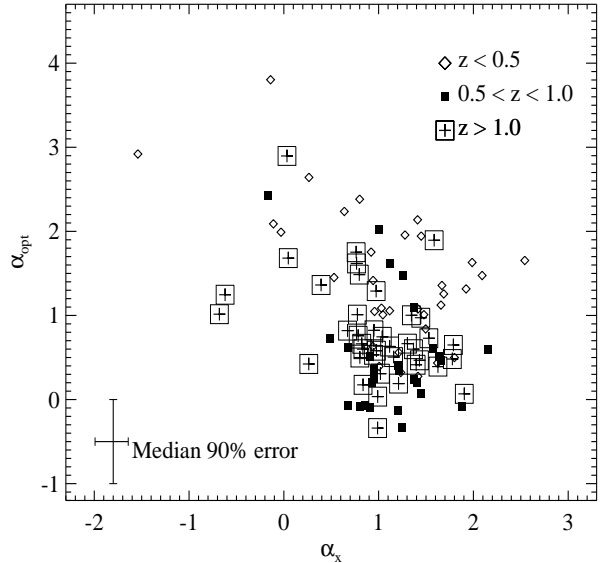

Figure 8. Optical power-law slope, α_{opt}, plotted as a function of the X-ray power-law slope, α_x. The data are plotted according to the redshift of the AGN, i.e. $z < 0.5$ are plotted as diamonds, $0.5 < z < 1.0$ are plotted as filled boxes and $z > 1.0$ as crosses within boxes.

when the sample is considered as a whole, however there appears to be a redshift dependence in the relationship (see Fig 8). At low redshifts, α_{opt} is likely to be affected by the host galaxy and thus may be soft relative to higher-z AGN (cf. Fig 4); indeed Fig 8 demonstrates that the $z < 0.5$ AGN are systematically displaced to softer values of α_{opt} relative to the higher redshift objects. When the data are divided into redshift bands, the correlation strengthens, e.g. at $z < 0.5$, p_{corr}=80 per cent (r_S=–0.4) while for $z > 0.5$, p_{corr} also rises to 80 per cent (r_S=–0.3). However, the strongest correlation is found in the high-z AGN, i.e. for $z > 1.0$,

p_{corr}=96 per cent (r_S=−0.5). The degree of correlation (as measured using the Spearman rank-order coefficient) is affected by the tendency of the data to cluster around α_x=1 (see Fig 3) and the relative paucity of very hard and soft α_x objects which is an expected consequence of the RIXOS selection criteria. Samples with a more homogeneous dispersion in α_x and improved measurements of the intrinsic slopes will provide a more definitive answer.

Nonetheless, even given the relatively basic methods for measuring α_x and α_{opt}, the data for these AGN show compelling evidence for a correlation between the two slopes. The correlation implies that when the optical continuum is hard, the soft X-ray slope is soft (and vice-versa) so that both the optical and X-ray slopes fall and rise towards the EUV together.

This is the first time that a relationship between the optical and X-ray slopes has been found. L94 found no correlation in their PG quasar sample, but since the RIXOS data suggest that α_{opt} changes only very slowly with α_x (see Fig 8), a sample covering a wide range in α_x and/or α_{opt} is essential to identify any trend; the L94 AGN were UV-excess quasars whose range in α_{opt} (−0.2 to 0.9) may have been too small for this correlation to be detected.

Together with the dependence of α_{ox} on α_x, these correlations are additional evidence linking the optical/UV BBB to the soft X-ray excess. In short, when α_x is soft, the optical continuum (α_{opt}) is hard and the optical-to-X-ray ratio (i.e. α_{ox}) is high. Conversely, when α_x is hard, α_{opt} is soft and α_{ox} is low.

3.3 Mean optical-to-X-ray continua

To illustrate the changes in the shape of the optical-to-X-ray spectrum, we have calculated three 'mean' spectra at different values of α_x, covering 6000 Å to 2 keV. The mean α_{ox}, α_{os} and α_{opt} were calculated in three bins centred on α_x=0.25, 0.95 and 1.65 and each covers an interval $\Delta\alpha_x$=0.7. Only AGN with redshifts in the range $0.25 < z < 3.25$ were used to avoid possible host galaxy contamination in the optical at low redshifts and the highest-z object whose X-ray and optical continuum slopes have relatively high errors.

The mean indices and the errors on the means are shown in Fig 9a-c and listed in Table 3. These were then used to construct the mean 'spectra' at α_x=0.25, 0.95 and 1.65 (Fig 9d; they have been normalized at 2.0 keV) and illustrate more clearly the changes in the spectra suggested by the data. When α_x is very soft, α_{opt} is hard and the spectrum is "convex" (indicated by the dashed line in Fig 9d), while when α_x is hard, α_{opt} is soft and the overall spectrum is "concave" (the dot-dashed line in Fig 9d).

4 MODELLING THE CONTINUUM

Recent work on the continua of Seyfert 1s and quasars has contributed much to our understanding of AGN spectra, especially with regard to the possibility of a single 'big bump'. Both WF and L94 identified a strong α_{ox} vs α_x correlation; WF suggested that changes in the flux of a big bump relative to an invariant underlying component could explain the spectral differences from source to source and that the shape of the big bump from the UV to soft X-rays showed little change.

Table 3. Mean optical and X-ray spectral indices ($0.25 \leq z \leq 3.25$)

	−0.1<α_x≤0.6	0.6<α_x≤1.3	1.3<α_x≤2.0
α_{ox}	1.10±0.05	1.13±0.02	1.21±0.02
α_{os}	1.62±0.12	1.21±0.04	0.99±0.04
α_{opt}	1.50±0.33	0.72±0.10	0.72±0.10

Errors quoted are the errors on the mean (i.e. $\sigma/(N-1)$, where N is the number of data points).

The overall changes in optical-to-X-ray continua of the RIXOS AGN (illustrated in Fig 9d) could also be interpreted as being due to the sum of two components; a big bump spectrum, whose flux varies significantly from source to source, and a relatively invariant underlying continuum (i.e. a similar model to that proposed by WF). If this model is to satisfy the full range of the observed RIXOS spectra, the underlying continuum must be concave with a break between 2500 Å and 0.2 keV (see the mean spectrum indicated by the dot-dashed line in Fig 9d; we stress that we have *no* information about the shape of spectrum between 2500 Å and 0.2 keV).

However, an underlying continuum of this form is difficult to reconcile with observations at longer and shorter wavelengths. The slope of the underlying continuum in soft X-rays (i.e. based on the RIXOS AGN with the hardest α_x) would be equivalent to $\alpha_x \sim 0$, which is significantly harder than the indices of Seyferts and quasars at higher energies [$\sim$2-50 keV; for Seyferts α_x=0.7 while for quasars, α_x is closer to 1.0 with small dispersions about the mean (Mushotzky, Done and Pounds 1993 and references therein)]. Also, an extrapolation of the rather soft optical continuum to longer wavelengths (equivalently $\alpha_{opt} \sim 2$ when $\alpha_x \sim 0$) predicts a very strong flux in the IR, whereas typically the continua of AGN spectra are generally harder with an $\alpha \sim 1$ extending down to $\sim$100μm (for examples see Elvis et al. 1994).

It is possible to have an underlying continuum of this shape *and* remain consistent with the IR and hard X-ray continua by assuming that the underlying continuum is a simple power-law which is absorbed predominantly in the optical/UV and soft X-ray regions, e.g. by cold gas and dust. However, it is in practice difficult to envisage a physical model where the nuclear power-law source lies behind significant amounts of cold, dusty gas, leaving the big bump-emitting region bare.

Thus we conclude that the changes in continuum shape for the RIXOS AGN cannot simply be due to either *1.* a continuum which is the sum of a power law and a big bump with different relative strengths, and which is unabsorbed; or *2.* a continuum which is the sum of an absorbed power law and an unabsorbed big bump.

Neither are the observed correlations consistent with a big bump component which 'shifts' between the optical and soft X-ray regions. In this case, when the big bump spectrum lies at relatively low frequencies (i.e. it is strong in the optical but weak in soft X-rays), we would expect a hard α_{opt} and a hard α_x; conversely when the spectrum lies at relatively high frequencies (i.e. weak in the optical but strong in soft X-rays), both α_{opt} and α_x would be soft. Thus we would expect to see a *correlation* of α_{opt} with α_x
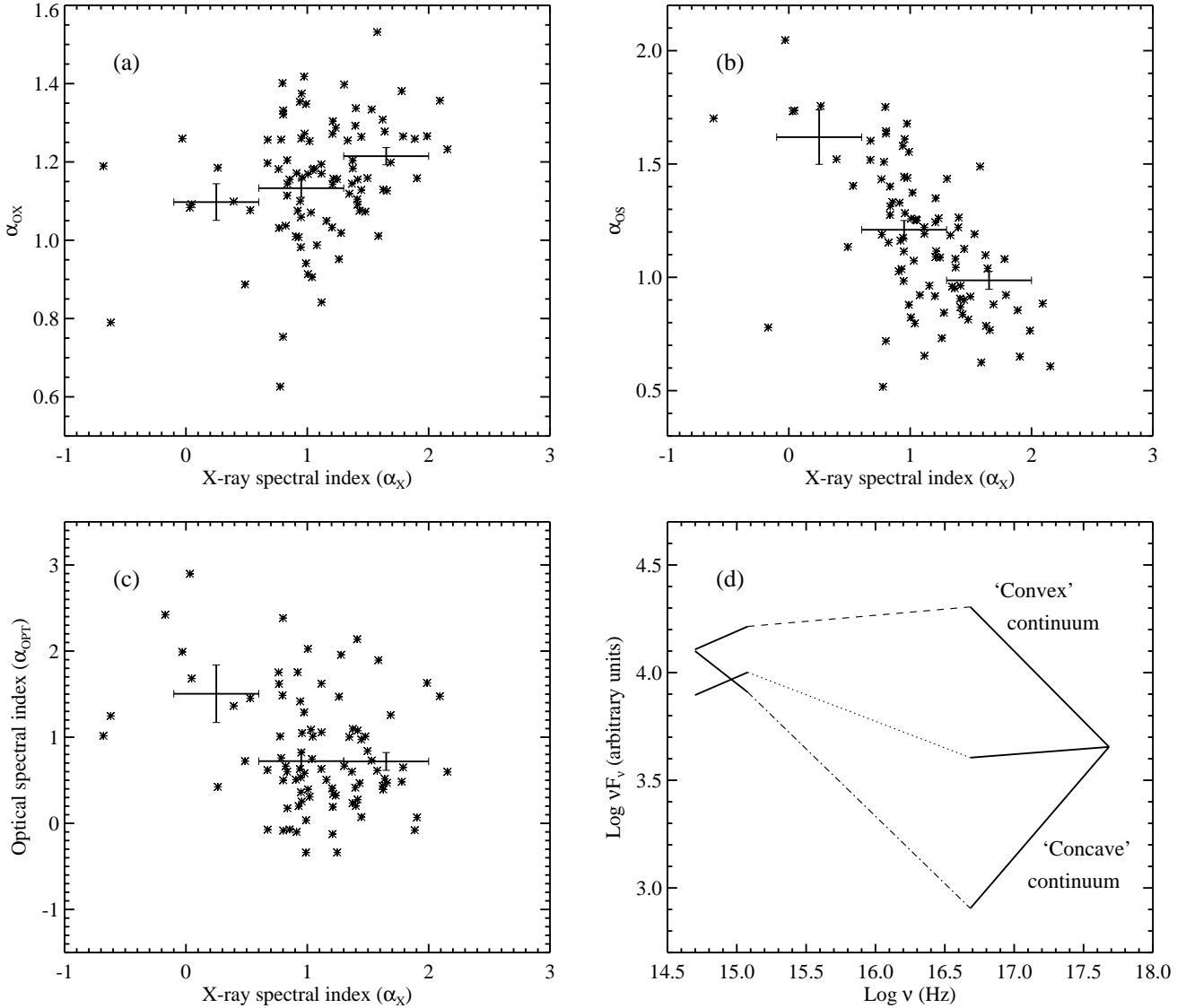
Figure 9 The calculation of three 'mean' RIXOS AGN spectra from 6000 Å-to-2 keV. (a)-(c) Data in the range z=0.25 to z=3.25. Also plotted as horizontal bars are the means in each of three equally spaced α_x bins for these data (vertical bars indicate the errors on the means; see Table 3). (a) α_{ox} plotted against α_x; (b) α_{os} plotted against α_x; (c) α_{opt} plotted against α_x. (d) Three mean continuum spectra calculated from the means shown in (a)-(c). Only the separate optical and X-ray slopes and their relative normalization are known; we have no information in the 2500 Å-to-0.2 keV region. The spectra may be identified by the broken lines joining the optical and X-ray regions; i.e. α_x=0.25 is indicated by the dot-dash line (also referred to as the "concave" spectrum), α_x=0.95 is indicated by the dotted line and α_x=1.65 (referred to as the "convex" spectrum) is shown by the dashed line.

rather than the *anti*-correlation observed. Examples of shifting spectra are AD models with different black hole masses and bremsstrahlung components with a range of temperatures.

4.1 Cold absorption

Instead we propose that the changes in continuum shape which are responsible for producing the observed correlations, may be primarily due to absorption of the entire intrinsic spectrum by cold gas and dust. The cold gas would be responsible for absorption in soft X-rays while the dust would be the source of absorption in the optical and UV.

The intrinsic spectrum may be the sum of a power-law and a big bump. The big bump temperature, power-law slope and big bump-to-power-law continuum flux ratio may also vary from source to source, introducing scatter into the data, however it is the absorption which results in the observed correlations.

To test whether this crude model is consistent with the observed spectra, the optical and X-ray spectral slopes and ratios were simulated by constructing a model for the intrinsic spectrum and modifying this for the effects of absorption by cold gas and dust. Throughout the remainder of this section, we investigate whether this model can predict the data which is actually observed, while the physical consequences

of such a model for AGN are discussed in Section 5. This is intended to be a preliminary assessment and consistency check of the model; a more rigorous treatment awaits a future paper.

The intrinsic spectrum in the model was assumed to be the sum of an underlying continuum and a big bump and its flux was fixed while the amount of absorption was varied. A simple power law with a slope of α=1.0 was adopted for the underlying optical-to-X-ray continuum; the chosen model for the big bump is discussed in Section 4.1.1. In soft X-rays, the Morrison and McCammon (1983) absorption cross-sections were assumed while in the optical and UV, the reddening curve of Cardelli, Clayton & Mathis (1989) was used. A Galactic dust-to-gas ratio [where E(B-V)=1.0 corresponds to an $N_{\rm H}$ of 6×10^{21} cm^{-2}; Ryter, Cesarsky & Audouze 1975; Gorenstein 1975] was assumed for the dust abundance. The model $\alpha_{\rm opt}$ was calculated by fitting a power-law to the model spectrum; the 2200 Å dust absorption feature was ignored in the fitting as this is rarely observed in the UV spectra of AGN (Cardelli & Clayton 1991; Mathis & Cardelli 1992). The X-ray spectral index was derived by first binning the model spectrum into three 'colours' which reflected the binning used in the analysis of the data (see Section 2.2), then fitting a power-law to these colours.

Because the AGN spectra sample such a wide range in z, it is necessary to include the effects of redshift on the model. The optical and X-ray slopes have been measured in fixed ranges in the frame of the *observer*, therefore they correspond to different parts of the *intrinsic* quasar spectrum, depending on z, and this must be taken into account when trying to reproduce the data. Therefore the models have been calculated at different redshifts (z=0.2, 0.5, 1.0, 1.5 and 2.5) to check that the predictions are consistent with the data. Both the optical and X-ray ranges were corrected by a factor of $1+z$ before the model indices were calculated.

4.1.1   *Choosing a model for the big bump*

To find an appropriate model for the big bump, we have compared the "convex" spectrum in Fig 9d (i.e. the mean $\alpha_{\rm x}$=1.65 RIXOS spectrum, which we assume to be dominated by the big bump) with several different models including ADs and bremsstrahlung spectra. The convex spectrum is much broader in wavelength than for many types of AD model, whether geometrically-thick (e.g. Madau 1988) or thin (e.g. Sun and Malkan 1989), although it does compare well with the modified Czerny & Elvis (1987) model of an AD which is surrounded by a hot ($T = 10^8$ K) corona.

A simple thermal bremsstrahlung spectrum with a temperature, $T_{\rm brem}$=1.2$\times10^6$ K also compares well with the convex spectrum; bremsstrahlung models have previously been used to fit the big bumps of other AGN with soft excesses, e.g. PG1211+143 was fitted with a $T_{\rm brem}$=8$\times10^5$ K spectrum (Barvainis 1993) and E1346+266 compared well with a bremsstrahlung model with $T_{\rm brem}$=7$\times10^6$ K (Puchnarewicz et al. 1994).

The AD-plus-corona and bremsstrahlung models are plotted in Fig 10 with the mean $\alpha_{\rm x}$=1.65 'observed' spectrum (an α=1.0 power-law has been added to the model spectra). In the subsequent modelling, for simplicity, we have used a thermal bremsstrahlung spectrum for the big
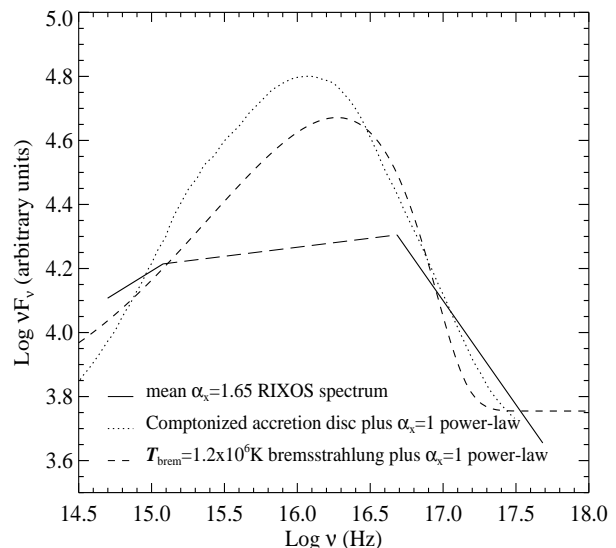

Figure 10. A comparison of the mean convex RIXOS spectrum (i.e. the mean $\alpha_{\rm x}$=1.65 spectrum from Fig 9d; plotted here as a solid/long-dashed line) with two models for the BBB and soft X-ray excess; *1.* the Czerny & Elvis (1987) model of an accretion disc surrounded by a hot ($T = 10^8$ K) corona (dotted line), and *2.* a $T_{\rm brem}$=1.2$\times10^6$ K simple bremsstrahlung spectrum (dashed line). An $\alpha_{\rm x}$=1.0 power-law has also been added to both models.

bump, although the AD-plus-corona provided an equally acceptable alternative.

4.2   **Finding the best fit**

In this section, we assess the ability of the model to reproduce the observed correlations between $\alpha_{\rm x}$ and $\alpha_{\rm ox}$ and between $\alpha_{\rm x}$ and $\alpha_{\rm opt}$. While we have searched for the best-fitting models over a wide range of parameter space (i.e. in $T_{\rm brem}$ and the relative normalization of the bremsstrahlung component), the model has not been allowed to converge formally, therefore the presence of other minima in the data are possible. This approach was considered adequate for the purpose of a first evaluation of the model.

In searching for the model which provided the best representation of the data at each redshift, we changed two of the parameters, $T_{\rm brem}$ and the flux in the bremsstrahlung component relative to the power law. The model was calculated over a grid of $T_{\rm brem}$ and big bump-to-power-law flux ratios and at each point in the grid, $T_{\rm brem}$ and the flux ratio were fixed while the intrinsic $N_{\rm H}$ was varied. The $\alpha_{\rm ox}$ versus $\alpha_{\rm x}$ and $\alpha_{\rm opt}$ versus $\alpha_{\rm x}$ distributions were fitted simultaneously and the goodness-of-fit was evaluated using the χ^2_ν statistic (taking into account the errors on $\alpha_{\rm ox}$ and $\alpha_{\rm opt}$; see Table 1). The 'best-fits' described throughout the remainder of the paper represent the points in the grid with the lowest χ^2_ν. The $\alpha_{\rm os}$ versus $\alpha_{\rm x}$ distribution is biased by a selection effect and may not be a real physical dependence (Section 2.1.2), therefore it was not included in the fits (although the predicted model has been compared with the data in the plots as a check for consistency). The models were only fitted to the data appropriate to the redshift assumed, i.e. the models at z=0.2, 0.5, 1.0, 1.5 and 2.5 were fitted to the data in the z=0-0.25, 0.25-0.75, 0.75-1.25, 1.25-1.75 and 1.75-3.5
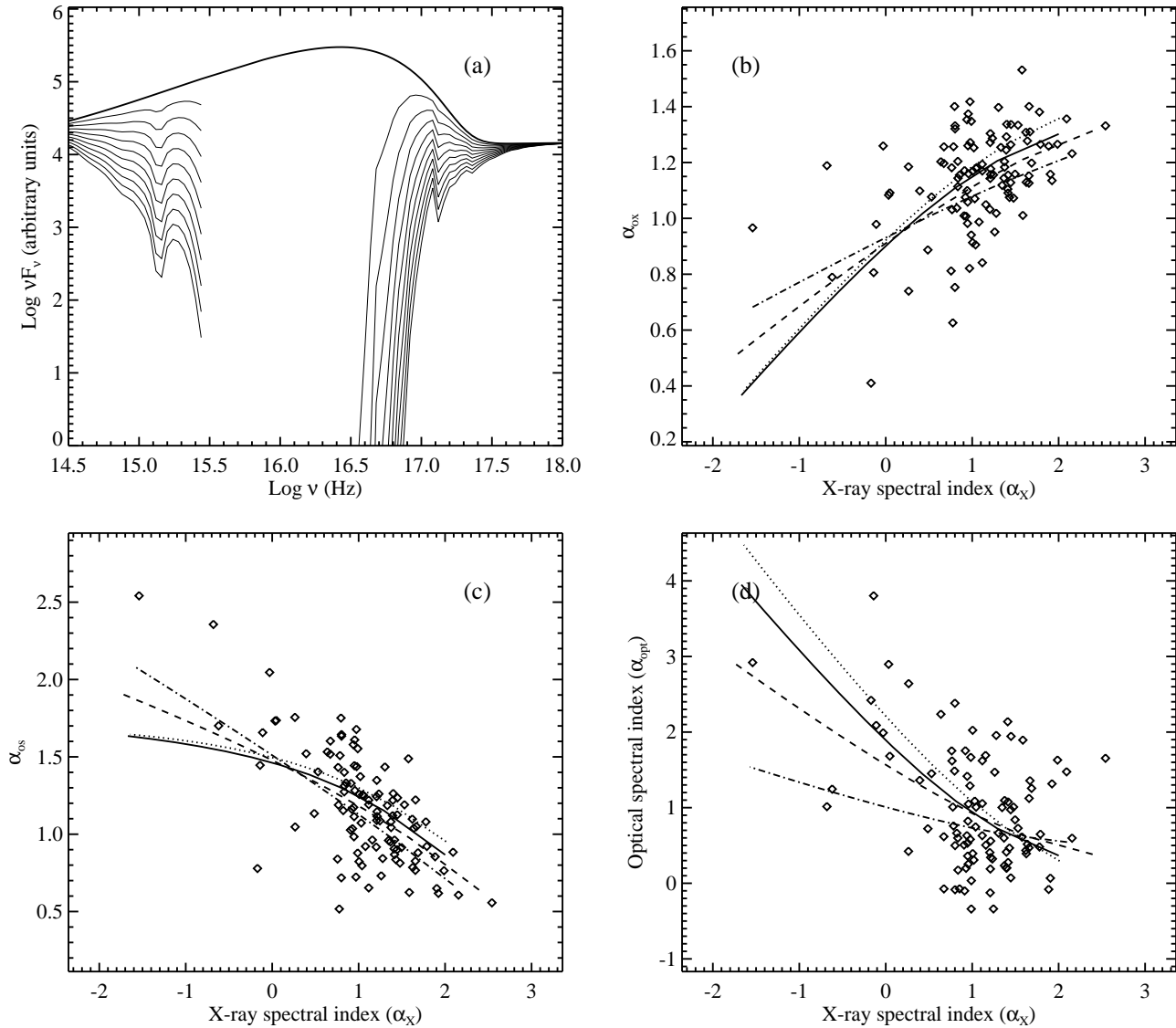
Figure 11. A comparison of the RIXOS AGN data with the model which assumes the sum of a bremsstrahlung spectrum and an α_x=1.0 power-law and which is absorbed by cold gas and dust. The flux in the power-law and the bremsstrahlung spectrum remain constant while the absorbing column density is varied; (a) illustrates the range of continua predicted by the z=1.0 model: the thick line is the unabsorbed spectrum while each curve plotted as a thin line represents absorption by an additional 6×10^{20} cm^{-2}. In (b)-(d), models are plotted for z=0.2 (dot-dashed line), z=0.5 (dashed line), z=1.0 (solid line) and z=1.5 (dotted line). Model spectral indices are compared with the data in (b) where α_{ox} is plotted against α_x; (c) α_{os} is plotted against α_x, and (d) α_{opt} is plotted against α_x. In all cases, the observed data are plotted as diamonds.

ranges respectively.

The 'best-fitting' models at all redshifts except z=2.5 are plotted in Fig 11 and show a good agreement with the data, considering the simplistic assumptions made. Parameters of the models are listed in Table 4; the normalization of the bremsstrahlung component relative to the power-law is expressed as $R_{0.2keV}$, the ratio of flux in the bremsstralung spectrum to flux in the power law at 0.2 keV.

There are very few differences between the best-fitting α_{ox} vs α_x models as the redshift changes, which is consistent with the observations (see Figs 4, 5 and 7, and Section 3.1). The model does predict however that for any given α_x, α_{opt} should be relatively soft at higher-z, whereas the observed

values for α_{opt} tend to be softer at *low-z* (i.e. $z < 0.5$; although this may be due to contamination by the host galaxy for which no corrections have been made). The slopes of the predicted α_{os} versus α_x models are harder than the observed data; this may be a consequence of the selection effect discussed in Section 2.1.2.

At higher redshifts ($z > 1.75$), the range of α_x is relatively small and the relationships between the indices may not be the same (Section 3.1), therefore we discuss these objects separately. When z is high, the model predicts that the effects of absorption in soft X-rays are lessened (because the strongly absorbed part of the spectrum has been shifted out of the observed range), while in the optical, the absorp-
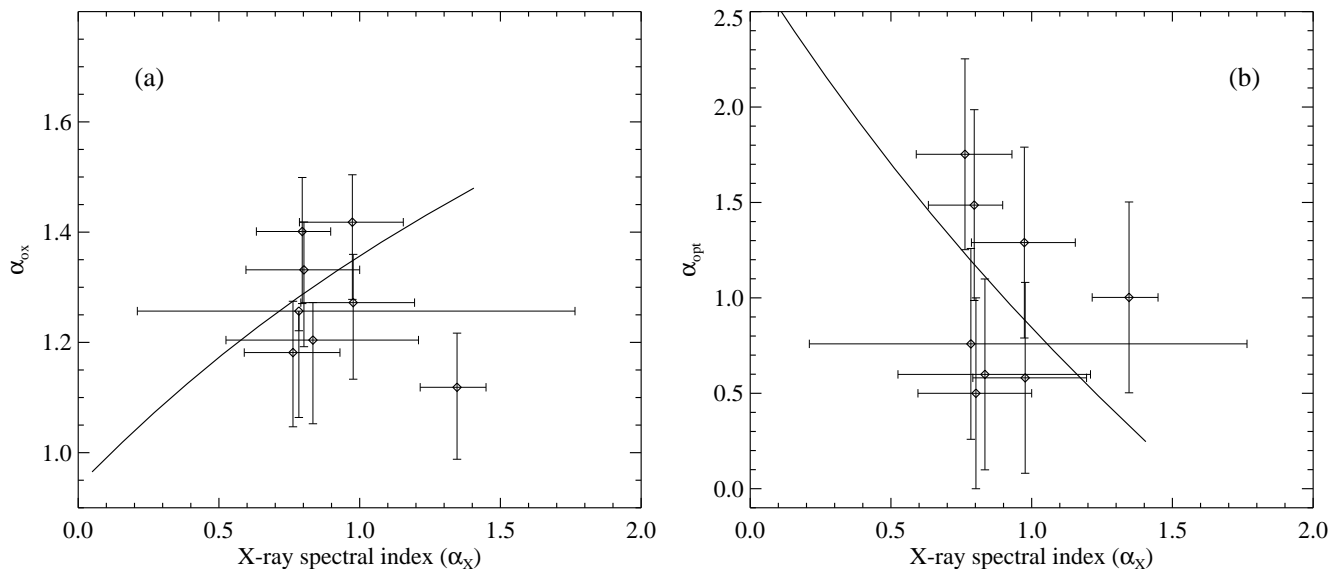
Figure 12. A comparison of the model predictions with the data for the high redshift ($z > 1.75$) AGN; *(a)* α_{ox} versus α_{x}, and *(b)* α_{opt} versus α_{x}. The model (plotted as a solid line) has a temperature, $T_{\mathrm{brem}}=1\times10^6$ K and $R_{0.2keV}=50$, and assumes a redshift of 2.5.

Table 4 Parameters of the best-fitting models to the RIXOS AGN continua (plotted in Figs. 11 and 12)

z	T_{brem} (1)	$R_{0.2keV}$ (2)	N_{H} (3)
0.2	1.7×10^6K	10	1.6
0.5	1.7×10^6K	20	4.0
1.0	1.3×10^6K	20	6.0
1.5	1.2×10^6K	30	7.0
2.5	1.0×10^6K	40	4.0

(1) Temperature of the bremsstrahlung component. (2) Ratio of flux in the bremsstrahlung component to flux in the power-law component at 0.2 keV. (3) Maximum column density of the gas used to produce the model in units of 10^{21} cm^{-2}.

tion has a greater effect (because the heavily-absorbed UV is shifted *into* range). Therefore, the scatter in α_{x} at high-z would be reduced while the range in α_{opt} and α_{ox} would remain relatively wide. In Fig 12 we compare the α_{ox} versus α_{x} and α_{opt} versus α_{x} distributions with the best-fitting model at z=2.5 (parameters of the model are listed in Table 4) and we find that the high-redshift data are consistent with the predictions of the model. Thus the model can predict the observed data from z=0 to $\sim$3.

4.2.1 Errors on the Galactic N_{H}

The measurements of α_{x} used in this analysis have already been corrected for N_{HGal}, therefore any absorption implied by the modelling is additional to this. In principle, this could be caused by errors on the assumed N_{HGal} rather than absorption external to our Galaxy. To test whether the changes in the continuum slopes of the RIXOS AGN could be due to errors on N_{HGal}, we have compared the N_{H} distribution implied by the model with the typical uncertainties on the Stark et al. (1992) measurements of N_{HGal}.

By default the model assumes that the gas and dust absorption occurs in the rest-frame of the quasar; to measure the equivalent *Galactic* column, the model was modified to assume that the absorption is entirely within the frame of the observer.

We found that the typical additional observer-frame column density suggested by the model would be $\sim 2 \times 10^{20}$ cm^{-2} (and this model also provided a poorer representation of the data, especially at high-z). Elvis, Lockman & Wilkes (1989) calculated a 1σ error on the Stark et al. measurement of N_{HGal} of 11 per cent for pointings at high Galactic latitude, implying typical errors on N_{HGal} for the RIXOS AGN of $\sim 2 \times 10^{19}$ cm^{-2}; this is significantly lower than the additional 'Galactic' columns implied by the model. Thus we conclude that the variations in continuum shape are not simply a reflection of the errors on the measurements of N_{HGal}.

4.3 Range of big bump temperature and strength

Although the correlations between α_{ox} and α_{x} and between α_{opt} and α_{x} are significant, there is still a large degree of scatter in the data. While the modelling suggests that the *correlations* may be due to absorption, the *scatter* may reflect a range in other parameters such as the temperature and relative normalization of the big bump. Therefore, by calculating models for different values of T_{brem} and the big bump-to-power-law ratio and comparing these with the observed distributions, we can find the approximate ranges of temperature and normalization implied by the model.

4.3.1 T_{brem}

To investigate the range of bremsstrahlung temperature, different models were calculated at low and high T_{brem} until they fell outside the regions occupied by the distributions of the spectral indices (i.e. α_{ox} versus α_{x} and α_{opt} versus

$\alpha_{\rm x}$). The normalizations and column densities were adjusted where necessary to provide the best comparison with the data.

The limits on the bremsstrahlung temperature implied by the model at a redshift of 1.0 are shown in Fig 13 and listed in Table 5, and show that a wide range in temperature can be accommodated (from 10^5 to 3×10^6 K). At lower temperatures, the bremsstrahlung spectrum does not reach far enough into soft X-rays to reproduce the soft excess, while at higher temperatures, the $\alpha_{\rm ox}$ is too low for any given $\alpha_{\rm x}$, as the big bump component shifts too far out of the optical range. Both upper and lower limits are constrained by the $\alpha_{\rm ox}$ versus $\alpha_{\rm x}$ distribution; the scatter in the observed $\alpha_{\rm opt}$ versus $\alpha_{\rm x}$ data falls outside these limits (at low and high $\alpha_{\rm opt}$) but because of the relatively high errors on the measurements of $\alpha_{\rm opt}$ we are unable to determine whether this is physically significant.

4.3.2   Ratio of big bump to power-law flux

A similar procedure was followed to estimate the range of the big bump-to-power-law flux ratio implied by the model. In this case, $T_{\rm brem}$ was fixed while the normalization of the bremsstrahlung spectrum was varied until the model fell outside the regions defined by the data. Only the column density was adjusted where necessary to extend the model to hard $\alpha_{\rm x}$.

The results (at $z = 1$) are shown in Fig 14 and are compared with the best-fitting model (parameters are listed in Table 6). When the bremsstrahlung normalization is zero, there is no soft X-ray excess or BBB and only sources with a relatively hard $\alpha_{\rm x}$ and soft $\alpha_{\rm opt}$ can be predicted by the model. At the other extreme when $R_{0.2keV}$ is very high, there is little change in the model for the predicted $\alpha_{\rm ox}$ and $\alpha_{\rm os}$ versus $\alpha_{\rm x}$ distributions, but at any given $\alpha_{\rm opt}$, the X-ray slope is much softer. This is because the bremsstrahlung dominates throughout the optical/UV so that the slope is unchanged by the flux in the big bump (except for very low normalizations), whereas in soft X-rays, the bremsstrahlung spectrum only dominates at relatively low X-ray energies (i.e. less than ~0.5 keV) and therefore its strength relative to the power-law has a much greater effect on the measured X-ray slope.

The model thus suggests that when $T_{\rm brem}=1.25\times10^6$ K (at $z=1.0$), $R_{0.2keV}$ can vary from 0 to ~1000. The upper limit is constrained by the $\alpha_{\rm opt}$ versus $\alpha_{\rm x}$ distribution (although we note that the absorption required is correspondingly high to predict any given $\alpha_{\rm x}$) but there is no lower limit (i.e. the model can accommodate AGN without big bumps).

5   DISCUSSION

We have presented the optical and X-ray continuum parameters of 108 X-ray selected AGN from the RIXOS survey (Mason et al. 1996). From the correlation analysis of this sample, we find significant evidence for relationships between $\alpha_{\rm ox}$ and $\alpha_{\rm x}$ and between $\alpha_{\rm opt}$ and $\alpha_{\rm x}$ (especially at $z > 1.0$). These suggest that as the 0.2-2 keV spectrum softens, the 2500 Å-to-2 keV ratio increases and the slope of the optical spectrum hardens. The trends apply over a wide range of $\alpha_{\rm x}$ for soft *and* hard X-ray slopes (i.e. from $\alpha_{\rm x}\sim0$ to 2.5) and

Table 5 Range of bremsstrahlung temperature at $z=1$: parameters of models shown in Fig. 13

$T_{\rm brem}$ (1)	$R_{0.2keV}$ (2)	$N_{\rm H}$ (3)
1×10^5 K	10^i	3.0
1.3×10^6 K	20	4.0
3×10^6 K	30	5.0

(1) Temperature of the bremsstrahlung component. (2) Ratio of flux in the bremsstrahlung component to flux in the power-law component at 0.2 keV. (3) Maximum column density of the gas used to produce the model in units of 10^{21} cm^{-2}. All models are calculated at $z=1.0$. ^{i} Ratio calculated at 0.02 keV; the 0.2 keV ratio ($R_{0.2keV}$) is 1×10^{-7}.

Table 6 Range of bremsstrahlung normalization at $z=1$: parameters of models shown in Fig 14

$T_{\rm brem}$ (1)	$R_{0.2keV}$ (2)	$N_{\rm H}$ (3)
1.3×10^5 K	1000	10.0
1.3×10^6 K	20	5.0
1.3×10^6 K	0	4.0

(1) Temperature of the bremsstrahlung component. (2) Ratio of flux in the bremsstrahlung component to flux in the power-law component at 0.2 keV. (3) Maximum column density of the gas used to produce the model in units of 10^{21} cm^{-2}. All models are calculated at $z=1.0$.

suggest that the overall 6000 Å-to-2 keV spectrum changes from convex to concave as $\alpha_{\rm x}$ hardens.

WF and L94 have also identified $\alpha_{\rm ox}$ versus $\alpha_{\rm x}$ correlations in their relatively soft X-ray samples and WF suggested that it is due to changes in the strength of a big bump relative to an underlying continuum. However, this explanation is not appropriate for the RIXOS sample (which extends to harder X-ray slopes than WF) because it implies that the underlying continuum from 6000 Å to 2 keV must be concave (see e.g. the dot-dashed line in Fig 9d) and a spectrum of this shape is difficult to reconcile with observations at longer and shorter wavelengths (Section 4).

We have illustrated the main differences between the WF, L94 and RIXOS AGN samples, by plotting $\alpha_{\rm ox}$ as a function of $\alpha_{\rm x}$ in Fig 15 (these have been corrected for the differences in the definition of $\alpha_{\rm ox}$ for the three samples, i.e. the WF and L94 $\alpha_{\rm ox}$s have been increased by 0.02 and 0.04 respectively; see Section 3.1.3). The figure shows that the WF objects are clustered towards high $\alpha_{\rm ox}$ and high $\alpha_{\rm x}$ relative to the RIXOS AGN; a similar and more extreme pattern is seen for the L94 objects. This would have led WF and L94 to draw different conclusions regarding the nature of the optical-to-X-ray continua in AGN, e.g. the WF data do not require the effects of absorption perhaps because they observed very few highly absorbed sources (with $\alpha_{\rm x}<1$), while L94 suggested that sources with a soft $\alpha_{\rm x}$ were weak in X-rays (i.e. $\alpha_{\rm ox}$ was high when $\alpha_{\rm x}$ was soft), yet Fig 15 shows that in both the WF and RIXOS samples, there are also many sources with a much lower $\alpha_{\rm ox}$ when $\alpha_{\rm x}$ is soft (i.e. the 2 keV flux is high relative to the optical and the X-ray spectrum is soft), implying a true soft X-ray 'excess' in
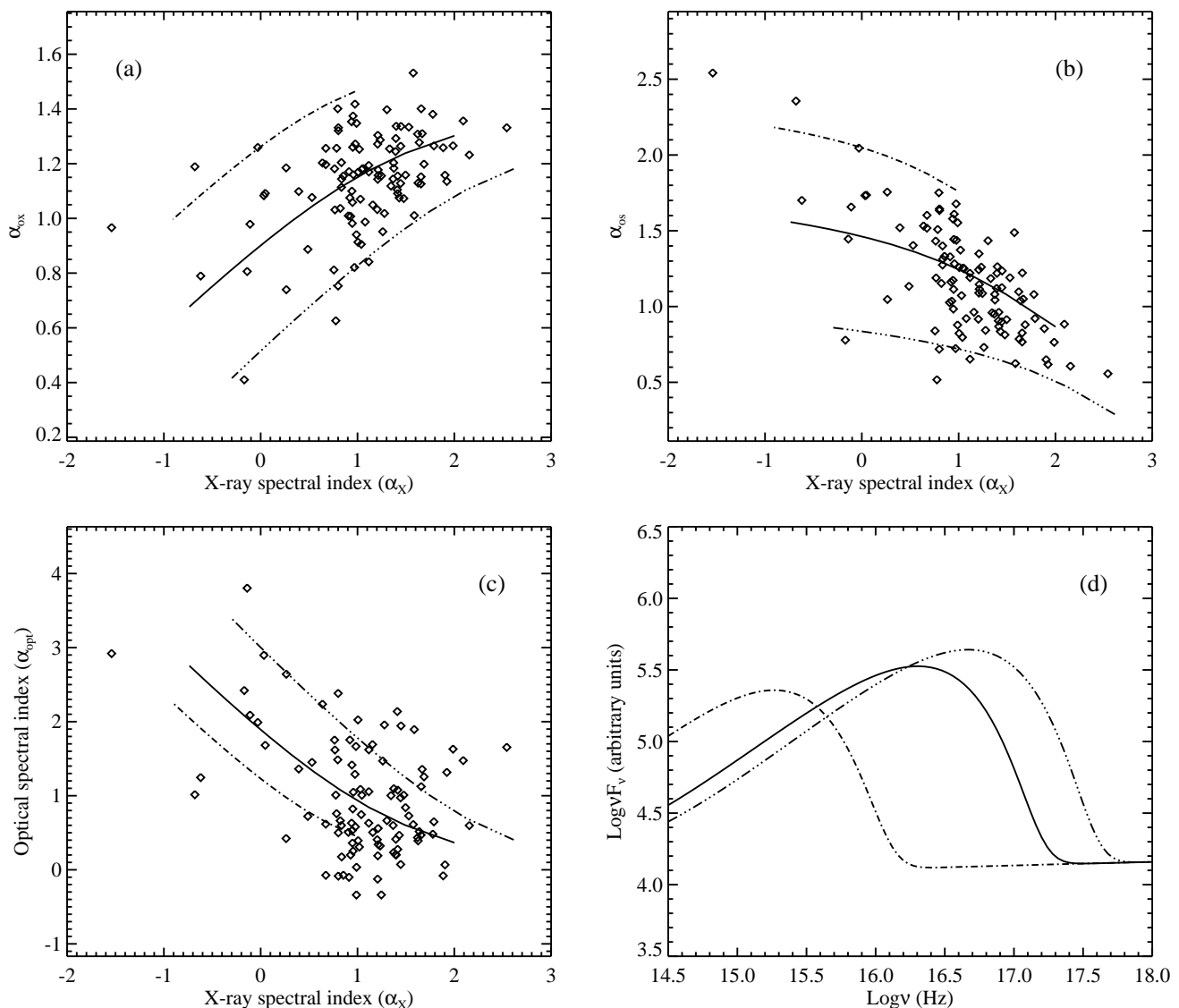
Figure 13. The range of T_{brem} at a redshift of 1.0 which is implied by the scatter in the observed data. Three different models are shown: for the dot-dashed line, $T_{\text{brem}}=10^5$ K; for the solid line, $T_{\text{brem}}=1.25\times10^6$ K; for the dot-dot-dot-dashed line, $T_{\text{brem}}=3\times10^6$ K. All three models are compared with *(a)* the observed α_{ox} versus α_{x} distribution; *(b)* the observed α_{os} versus α_{x} distribution; *(c)* the observed α_{opt} versus α_{x} distribution. The three unabsorbed model spectra are plotted in *(d)*.

these AGN.

These differences are largely a consequence of the selection methods, i.e. the PG quasars used by L94 were selected by the strength of their UV excess, thus they tend to be optically-bright and -hard, while the WF objects are bright in soft X-rays (0.08-2.4 keV) and therefore X-ray-bright and generally X-ray-soft. The RIXOS sample is itself restricted by its selection criteria (i.e. by the strength of the 0.4-2.0 keV emission), therefore its properties can only be said to be typical of objects which are relatively strong in medium X-rays (i.e. at ∼2 keV in the quasar rest-frame). Ultra-soft X-ray objects like E1346+266 and RE J1034+396, which have very soft *ROSAT* spectra yet little or no flux above ∼1 keV (Puchnarewicz et al. 1994; Puchnarewicz et al. 1995), would be selected against in this sample for instance; as would AGN which are heavily absorbed through cold gas.

As an explanation for the observed trends in the RIXOS AGN, we have proposed that the correlations are due to the effects of moderate absorption by cold gas and dust. It is possible that the results are also reproducible by a dusty warm absorber (see e.g. Mathur et al. 1994; Brandt, Fabian and Pounds 1996), but the additional parameters required for the fits are not justified by the quality of these data. This hypothesis has been tested using simple combinations of power laws and bremsstrahlung spectra which have been modified for the effects of dust and gas absorption. We find that the model is consistent with the data up to $z \sim 3$ (this is effectively the limit of the sample).

However, the model must also be judged by its ability to reproduce the spectra of AGN which lie outside the RIXOS parameter space, such as ultra-soft X-ray sources and the PG quasars (see Fig 15), which are relatively quiet
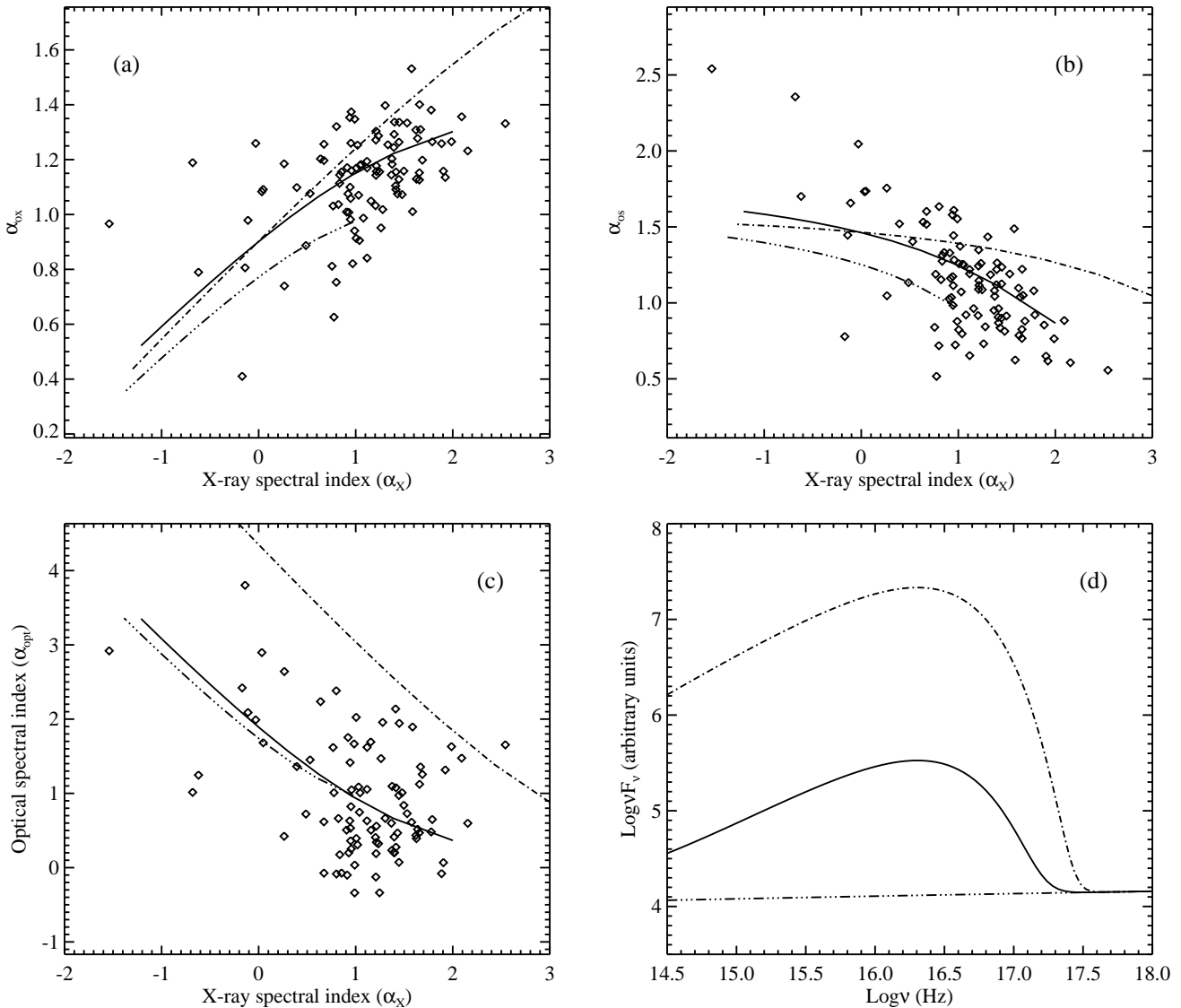
Figure 14. An illustration of the effect of changing the strength of the bremsstrahlung component relative to the underlying power law. Three different models (with z=1.0) are shown and compared with the data: for the dot-dot-dot-dashed line, there is no bremsstrahlung component; for the solid line, the $R_{0.2keV}$=20; for the dot-dashed line, $R_{0.2keV}$=1000. All three models have $T_{\rm brem}$=1.25×10^6 K and are compared with (a) the observed $\alpha_{\rm ox}$ versus $\alpha_{\rm x}$ distribution; (b) the observed $\alpha_{\rm os}$ versus $\alpha_{\rm x}$ distribution; (c) the observed $\alpha_{\rm opt}$ versus $\alpha_{\rm x}$ distribution. The three unabsorbed model spectra are plotted in (d).

in X-rays. We have fitted our model to the L94 sample of PG quasars, finding a best-fit when $T_{\rm brem}$=6×10^5 K and $R_{0.2keV}$=10, which reproduces the optical and X-ray slopes as well as the optical-to-X-ray ratio (see Fig 16). The temperature is lower than that required for the RIXOS AGN but $R_{0.2keV}$ is the same (see Table 4); the amount of cold absorption required is very small (a maximum of 3×10^{20} cm^{-2}). With regard to ultra-soft X-ray sources, we note that the optical-to-X-ray spectrum of the ultra-soft X-ray quasar E1346+266 also compares well with an unabsorbed bremsstrahlung spectrum ($T_{\rm brem}$=7×10^6 K; Puchnarewicz et al. 1995), in agreement with our model. However for the lower-luminosity ultra-soft Seyfert 1 galaxy RE J1034+396, a bremsstrahlung plus power-law provided a poor fit to the data (Puchnarewicz et al. 1995), thus while this model can

be extended to some ultra-soft X-ray AGN and UV-excess quasars, it may perhaps be inappropriate for lower luminosity ultra-soft objects like RE J1034+396. However given the idiosyncrasies of individual objects, more stringent tests must be made using higher quality data before any conclusions can be drawn at this stage.

We now discuss the implications of the model for an optical-to-soft X-ray big bump and for the presence and location of dusty, cold gas in AGN.

5.1   The origin of the BBB

The correlations in the data suggest that the BBB and the soft X-ray excess are either part of the same component (the 'big bump') or that they are separate but subject to the
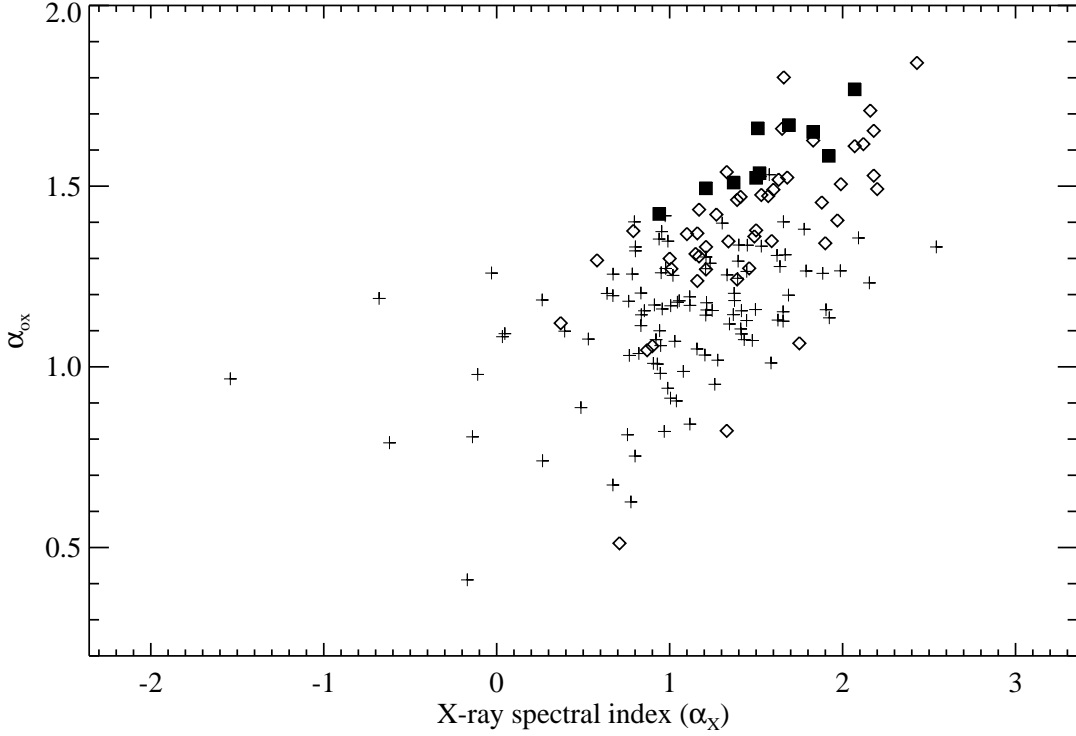
Figure 15. The distribution of α_{ox} versus α_{x} for the RIXOS AGN (crosses) compared with that of the WF (diamonds) and L94 (squares) samples. The WF and L94 data have been corrected for the differences in the definitions of α_{ox} between all three samples (see Section 3.1.3).
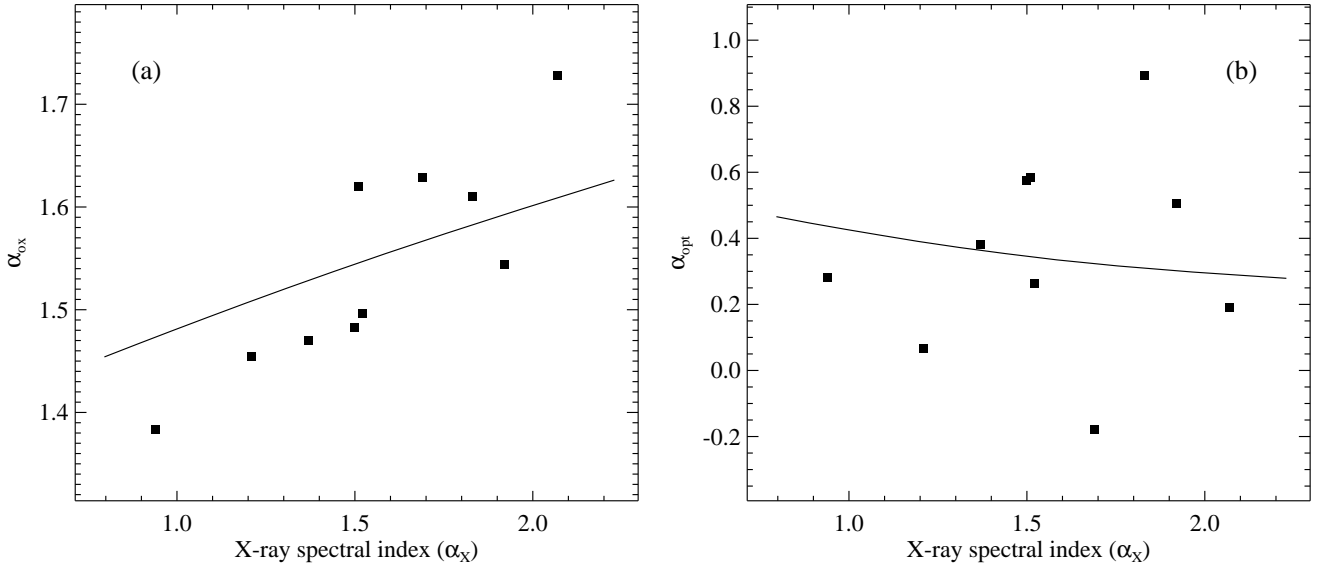

Figure 16. The L94 data (plotted as squares) compared with the best-fitting absorption model; (a) α_{ox} versus α_{x}, and (b) α_{opt} versus α_{x}. The model (plotted as a solid line) assumes a redshift of 0.2 (the mean redshift of the L94 sample) and has a temperature, $T_{\mathrm{brem}} = 6 \times 10^5$ K, $R_{0.2keV} = 10$ and uses a range of N_{H} from 0 to 3×10^{20} cm^{-2}.

same external influences. In the modelling, we used a single optical/soft X-ray big bump and this was demonstrated to provide a good representation of the data, therefore throughout this section we have assumed a big bump as the origin of the BBB and the soft X-ray excess.

5.1.1 Accretion discs

The optically-thick AD models are a natural assumption for the origin of the BBB and ADs have been successfully used to reproduce optical-to-X-ray AGN spectra (e.g. Arnaud

et al. 1985; Czerny & Elvis 1987; Sun & Malkan 1989), even in extreme cases such as the EUV-bright Seyfert 1 galaxy RE J1034+396 (Puchnarewicz et al. 1995). Although some AD models are not appropriate for the optical/soft X-ray big bump in the RIXOS AGN (Section 4.1.1), we find that the Czerny & Elvis (1987) model of an AD with a surrounding hot ($T = 10^8$ K) corona does compare well with the most convex (i.e. the mean α_x=1.65 spectrum indicated by the dashed line in Fig 9d) of the mean spectra. It is similar in shape to the bremsstrahlung spectrum which was successfully used in the modelling.

The AD corona is optically thin and cooled by inverse Compton scattering so that the high energy tail of the disc spectrum hardens and extends to higher energies. The geometry of the corona is not well constrained, for example it may form a thin 'skin' around the disc or be large and spherical. If the optical depth of a large corona is high ($\tau \sim 1$), then the model's prediction that soft X-ray excesses are only observed from ADs observed face-on, is relaxed (Czerny & Elvis 1987).

The Czerny & Elvis model shown in Fig 10 has a black hole mass of 10^8 M$_\odot$. With the naive assumption that the black hole mass scales inversely with the square root of the temperature (this applies in the simple thin disc approximation, e.g. Pringle 1981), then the range of $T_{\rm brem}$ implied by the model (i.e. $10^5 - 3 \times 10^6$ K at z=1) suggests black hole masses of $\sim 10^6 - 10^9 M_\odot$ for an equivalent AD model. Furthermore, as the redshift of the AGN increases, the temperature of the big bump tends to decrease (see Table 4). In the accretion disc models, the temperature of the disc is determined by the mass of the black hole and is lower when the black hole's mass is high. Thus if the big bump spectrum is produced by an accretion disc, then our model favours more massive black holes at higher redshifts. A similar pattern (i.e. low-temperature ADs at high-z) would be expected in order for the AD model to be consistent with the restrictions imposed by the Eddington limit.

5.1.2 Optically-thin gas

The bremsstrahlung model for the big bump has many attractive features which make it a viable alternative to the more popular, optically-thick AD (Barvainis 1993). For example, it can predict observed quasar continuum slopes in the optical ($\alpha_{\rm opt}\sim$0.2-0.3, e.g. Neugebauer et al. 1987) without the need for an extension of the X-ray power law into the optical to match the observed spectra; an additional power-law component is often required for AD models. Also, if the geometry of the gas is toroidal, it can produce linearly polarized light similar to that which is often observed (see Barvainis 1993 and references therein).

A bremsstrahlung spectrum has been assumed for the big bump in the modelling and we find that this successfully reproduces the observed spectral indices (i.e. $\alpha_{\rm ox}$, $\alpha_{\rm opt}$ and α_x). Although our model assumes that the X-ray power-law component continues down to $\sim$10000 Å, the bremsstrahlung spectrum dominates over the power law in the optical so that, in most cases, the removal of the power law longward of the EUV would make no significant difference to the model fits. The optical extension to the power-law *is* required however when the total flux in the bremsstrahlung component is weak relative to the X-ray

power-law (see, for example, the extreme case in Fig 14 where there is no bremsstrahlung component).

The scatter in the correlations observed in the RIXOS AGN may be satisfied by differences in the intrinsic $T_{\rm brem}$ and in the relative normalization of the big bump to the underlying continuum. The best-fitting temperature of the gas ($T_{\rm brem}\sim 10^6$ K) would be high enough to make the Lyman edge very weak and therefore difficult to detect (Barvainis 1993), which is consistent with observations (e.g. Antonucci, Kinney & Ford 1989; Koratkar, Kinney & Bohlin 1992).

One problem with an optically-thin origin of the big bump is its ability to reproduce the very short-timescale variability observed in some AGN, although Barvainis (1993) demonstrated that many small, free-free emitting cloudlets may have a source size as small as 1 lt-hr across.

5.1.3 Reprocessing in cool clouds

In the cool clouds model, the primary quasar spectrum is reprocessed by cool, dense clouds which lie close to, and perhaps even within, the central continuum emitting source (Guilbert & Rees 1988; Ferland and Rees 1988). The clouds absorb soft and medium X-rays and re-emit them in the optical/UV. This model may, for certain values of the cloud density and filling factor, predict observed AGN features such as the BBB and the soft X-ray excess, and has already been invoked to explain the medium-to-hard-X-ray spectra observed in Seyfert galaxies (Nandra & George 1994).

Barvainis (1993) has suggested that in principle, it is possible for the reprocessed optical/UV continuum to be optically-thin, thus the reprocessing (cool) clouds themselves may produce the big bump spectrum observed. The temperature of the free-free spectrum in this case would be $\sim 10^5 - 10^6$ K, which is similar to that implied by our modelling ($\sim 10^5 - 3\times10^6$ K), and the clouds must have relatively low densities ($N < 10^{15}$ cm^{-3}; Barvainis 1993), although not so low that the free-free emitting source becomes very large.

5.2 The absorbing medium

The model for the RIXOS AGN optical-to-X-ray continua described in Section 4.1, suggests that cold gas with a roughly Galactic gas-to-dust ratio and moderate ($N_{\rm H}\leq 5 \times 10^{21}$ cm^{-2}) column density lies along the line of sight to the quasar nucleus. Similar levels of intrinsic absorption have been observed in other AGN, e.g. in the quasar 3C109, Allen & Fabian (1992) found evidence of cold gas with a column density of 5×10^{21} cm^{-2} and a Galactic dust-to-gas ratio, while Mathur et al. (1994) have shown that the X-ray and UV spectra in 3C 351 are absorbed by a highly ionized outflow with a column density of 1-2$\times10^{22}$ cm^{-2}.

Based upon the parameters of the gas suggested by the modelling presented in Section 4, we now explore the nature of a possible cold absorbing medium in the RIXOS AGN and whether the results of the modelling can be consistent with the emerging picture of quasar and Seyfert nuclei.

5.2.1 Geometry of the gas

A 'first-order' indication of the covering factor of this dusty gas may be derived from the distribution of the intrinsic $N_{\rm H}$

which is implied by the modelling.

For any given model column density ($N_{\rm Hmod}$), the absorbed bremsstrahlung-plus-power-law model makes a prediction of the slope of the X-ray spectrum ($\alpha_{\rm xmod}$); $\alpha_{\rm xmod}$ is plotted as a function of $N_{\rm Hmod}$ in Fig 17a for the best-fitting models at redshifts from 0.2 to 2.5. Therefore, by using the *observed* $\alpha_{\rm x}$ and interpolating between the points of the function (appropriate to the redshift of that AGN), the amount of absorbing material intrinsic to the AGN ($N_{\rm Hint}$) may be derived. The data were thus divided into redshift bins (i.e. z=0-0.25, 0.25-0.75, 0.75-1.25, 1.25-1.75 and 1.75-3.5) and $N_{\rm Hint}$ was calculated for each AGN by interpolating between the corresponding $\alpha_{\rm xmod}$ vs $N_{\rm Hmod}$ functions (i.e. the z=0.2, 0.5, 1, 1.5 and 2.5 curves respectively).

The resulting distribution of $N_{\rm Hint}$ is shown in Fig 17b; these represent the column densities of the absorbing gas and dust intrinsic to the AGN and are *in addition* to $N_{\rm HGal}$. It shows a peak at $N_{\rm H} < 10^{21}$ cm^{-2} and implies that approximately one-third of the RIXOS AGN lie behind columns $\geq 10^{21}$ cm^{-2}.

When considering the distribution of $N_{\rm Hint}$, a number of points should be borne in mind. Firstly, the sample used in this paper is not fully complete, although the $\alpha_{\rm x}$ distribution of these sources is not significantly different from that of the complete RIXOS survey (Mittaz et al. 1996). Secondly, the defining criteria of the sample select against very soft sources which have little or no flux above 0.4 keV. However, based on the number of AGN in the Ultra-Soft Survey (Thompson & Córdova 1994) which have no significant emission above 0.5 keV, and comparing this with the AGN from the *Einstein* Extended Medium Sensitivity Survey (Gioia et al. 1990; Stocke et al. 1991), we estimate that only ∼10 very soft sources have been omitted. Finally, the RIXOS sample will not include heavily absorbed sources which have insufficient 0.4-2.0 keV flux to be detected, therefore at relatively high values of $N_{\rm Hint}$ (e.g. higher than ∼ 10^{21} cm^{-2}), the distribution in Fig 17b should be considered a lower limit.

Taking into account these restrictions on the sample, we can estimate the proportion of sources which are relatively unabsorbed (i.e. with $N_{\rm Hint} < 10^{21}$ cm^{-2}). Assuming (naively) that this distribution is typical of the AGN population in general, we find that 67 out of 108 sources are 'unabsorbed' (from Fig 17), which gives a covering factor for the absorber of ∼0.3. Allowing for a possible 10 missing ultra-soft X-ray sources makes no significant difference to the covering factor, but as we have made *no* allowance for AGN which are too strongly absorbed to be detected, this must be considered a very conservative lower limit. Thus geometries of the gas where the covering factor is relatively high, e.g. spherical and toroidal distributions, are favoured while models with a small covering factor (less than ∼0.1), e.g. thin discs, are unlikely.

A thick torus

If the gas is contained within a geometrically-thick torus, then the range of absorbing columns implied by the model may be due to orientation effects if the amount of gas along the line of sight to the nucleus changes with the 'viewing angle' (the angle between the line of sight and the axis of the torus). For example, if the density of the gas decreases with increasing distance from the plane of the torus
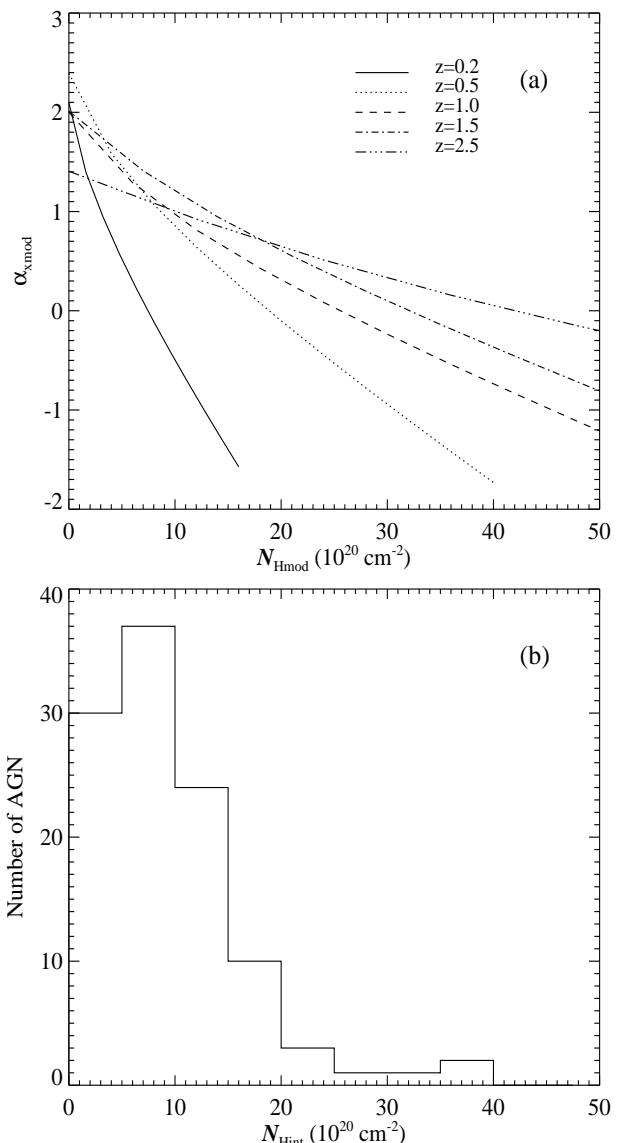

Figure 17. (a) The model $\alpha_{\rm x}$ at z=0.2, 0.5, 1.0, 1.5 and 2.5 (solid, dotted, dashed, dot-dashed and dot-dot-dot-dashed respectively) calculated from the best-fitting absorbed bremsstrahlung plus power-law models at those redshifts (see Section 4.1), and plotted as a function of the assumed input column densities. (b) The distribution of inferred intrinsic column densities for the RIXOS AGN ($N_{\rm Hint}$; solid line) calculated using the models plotted in (a) (i.e. using bins of z=0.0-0.25, 0.25-0.75, 0.75-1.25, 1.25-1.75 and 1.75-3.5 respectively). These represent the column densities which would be intrinsic to the AGN themselves and are in addition to any Galactic absorption.

(whether it is due to fewer clouds, less dense clouds or a less dense, smoothly distributed gas), then the amount of absorption observed would increase as the viewing angle increases. Otherwise, if the density remains constant, then the azimuthal profile of the torus may be such that the path length through the torus changes with the viewing angle. In this orientation-dependent model then, when the torus is observed relatively face-on, there would be very little absorption and $\alpha_{\rm x}$ is soft. As the viewing angle increases, the amount of cold gas along the line-of-sight increases and $\alpha_{\rm x}$

hardens.

Alternatively, the range of $N_{\rm Hint}$ may simply indicate that absorbing tori in AGN have a wide range of optical depths. Note that if the torus is made up of individual clouds, then the clouds must be able to have low column densities ($< 10^{21}$ cm^{-2}) in order to produce the small columns observed.

Spherical

If the gas is spherically distributed, then the observed range in $\alpha_{\rm x}$ reflects a range in the column density of the absorbing material. The distribution in Fig 17 would then imply that most RIXOS AGN are surrounded by gas with columns of $\sim 10^{21}$ cm^{-2}.

5.2.2   Location of the gas

The presence of dust places limits on the location of the gas, since the *minimum* radius at which dust grains sublime ($r_{\rm min}$) is given by $r_{\rm min} \simeq 0.20 L_{46}^{0.5}$ pc, where L_{46} is the bolometric luminosity in units of 10^{46} erg s^{-1} (Laor & Draine 1993). For the RIXOS AGN then, the smallest radius at which dust can survive is the order of a parsec, which places the dust beyond the broad line region (BLR). Thus the most likely locations of the dust are *(1).* the narrow line region (NLR), *(2).* the dusty molecular torus, which lies between the BLR and NLR, *(3).* the host galaxy and *(4).* intervening galaxies along the line of sight.

NLR

It has been suggested that dust lies within the NLR itself (e.g. Laor & Draine 1993). The covering factor of the NLR is very small however ($\sim$0.01) and since the distribution of $N_{\rm Hint}$ implies that a large fraction of the RIXOS AGN are absorbed, we conclude that the NLR is an unlikely source of the absorbing medium which produces the continuum changes.

Molecular torus

It has been proposed that a dusty, molecular torus lies between the BLR and NLR of many Seyfert galaxies (see e.g. Antonucci 1993 for a review). This torus is probably geometrically-thick [the ratio of the height (h) to the inner radius (r), is h/r, is $\sim$0.7, and $r \sim$1 pc] and has a high column density ($N_{\rm H} \geq 10^{24}$ cm^{-2}; Krolik & Begelman 1988). It is made up of clouds which individually have a large column density (i.e. $N_{\rm H} \geq 10^{24}$ cm^{-2}) and the torus has a cloud covering factor $\sim$1.

A torus of this kind is not possible as the source of absorbing gas in the RIXOS AGN, because the column density of individual clouds is much higher than that implied by the modelling, so that observed AGN continua would be completely unobscured or very strongly absorbed; in most cases we observe moderate absorption (i.e. $N_{\rm Hint} \sim 10^{21}$ cm^{-2}). However, if the Eddington luminosity of an AGN is high, the torus might instead be optically thin or geometrically thin (Krolik & Begelman 1988). We have ruled out a geometrically-thin absorber on the basis of the $N_{\rm Hint}$ distribution (Fig 17 and Section 5.2.1); a geometrically-thick torus, subject to the limitations discussed in Section 5.2.1, is possible however if the clouds have a low $N_{\rm H}$ ($< 10^{21}$ cm^{-2}).

Host galaxy

The column densities implied by the modelling are typical of the interstellar medium in the disc of our own Galaxy ($\sim 10^{21}$ cm^{-2} in a direction perpendicular to the plane of the disc; Stark et al. 1992), however absorption by the galactic disc local to the AGN is unlikely as the covering factor is small. Cold gas and dust in the bulge of spiral galaxies (which are the typical hosts for Seyfert 1 nuclei) and in ellipticals may produce the absorption implied; this would suggest a spherical distribution of the gas.

Intervening galaxies

It is also possible that the quasar spectra are absorbed through relatively face-on galaxies along the line of sight which are too faint to be seen. Spiral galaxies would be the most likely absorbers as they contain a higher HI mass than ellipticals or lenticulars (Rao & Briggs 1993). Any absorption by external galaxies close to high-redshift quasars would be difficult to measure in X-rays because the strongest effects of the absorption are shifted out of the observed range; the absorption we measure would be dominated by relatively nearby (i.e. low-z) galaxies. Nonetheless, we would expect to see a trend towards more heavily absorbed AGN as the redshift increases, yet there is no hardening of $\alpha_{\rm x}$ with z for the RIXOS AGN (Fig 4, this paper; Mittaz et al. 1996).

Although it is difficult to measure this kind of absorption in X-rays due to the redshift effect, it should be easier in the optical because the shorter wavelength regions, where the dust absorption is higher, are moved into the observer-frame, making absorption easier to detect. In this case, the optical slope would soften with increasing z, yet again, we find no significant changes of $\alpha_{\rm opt}$ with z (for $z > 0.25$). Thus we conclude that absorption by intervening spiral galaxies is unlikely.

5.3   The unified AGN model

In the 'hidden Seyfert 1' picture of a Seyfert 2 galaxy, some (if not all) Seyfert 2s are actually Seyfert 1 nuclei viewed through the dusty molecular torus (e.g. Miller & Goodrich 1987); this is a part of the 'unified AGN model' which essentially aims to explain the wide range of AGN properties by orientation effects (see e.g. Antonucci 1993 and references therein). We now speculate on an extension of this model to the quasar population in the light of the RIXOS results.

If indeed the RIXOS AGN are absorbed as we propose, then what we might be seeing is a mixture of type 1 and type 2 quasars (analogous to type 1 and type 2 Seyferts) whose X-ray and optical spectra are modified by a dusty torus. The torus has a low column density, (perhaps as a consequence of the relatively high luminosity of the quasars), low enough to modify the optical-to-X-ray continuum but still allowing much of the broad permitted line emission to escape. Thus most quasars would be classified as type 1s based on their optical spectra, even though their nuclear emission is viewed through the torus (as is assumed for Seyfert 2s). This would explain the rarity of 'type 2' quasars (i.e. quasars with narrow permitted and forbidden lines) since the BLR is not always completely absorbed by the torus.

6   SUMMARY

We have used the RIXOS AGN to probe the nature of the optical-to-X-ray continuum in a large sample of X-ray se-

lected Seyfert 1s and quasars. The sample provides a wide range in parameter space, i.e. in luminosity, X-ray spectral slope and optical-to-X-ray ratio, over which to search for relationships between the optical and X-ray continua. We confirm the α_{ox} vs α_x correlation previously reported by WF and L94, and identify anti-correlations between α_{opt} and α_{ox} and between α_{opt} and α_x (especially at $z > 1.0$), suggesting that the optical and X-ray slopes fall and rise towards the EUV together.

These relationships imply overall changes in spectral shape from convex (when α_x is soft) to concave (when α_x is hard; see Fig 9d). They also suggest that the BBB and the soft X-ray excess are strongly dependent and they may be part of the same optical-to-soft X-ray 'big bump'. The changes in the mean optical-to-X-ray continua are not consistent with a component which shifts between the optical and X-ray regions, e.g. ADs or bremsstrahlung spectra with a range of temperatures. Although these changes might be produced by a big bump with varying strengths superposed on a relatively invariant underlying continuum, the underlying continuum must be either (1) concave from 6000 Å to 2 keV (like the dot-dashed continuum in Fig 9d) yet have $\alpha \sim 1$ at lower and higher frequencies, or (2) absorbed by cold gas and dust while the BBB and soft X-ray excess are completely unabsorbed: we conclude that both are unlikely.

We have proposed instead that the changes are due to absorption of the entire intrinsic quasar spectrum by cold gas and dust and have demonstrated the viability of this idea from $z=0$ to ~ 3 by creating models of the absorbed continua. The model assumes that the intrinsic spectrum is the sum of an $\alpha=1$ power law and a bremsstrahlung spectrum. The temperature of the bremsstrahlung component favoured by the modelling is $\sim 10^6$ K and the scatter in the data implies a range in T_{brem} of $\sim 10^5$ K to 3×10^6 K. A wide range in the strength of the big bump is also permitted by the model, e.g. at $z=1$ and for $T_{brem}=1.25 \times 10^6$ K, the ratio of flux in the bremsstrahlung spectrum to that in the power-law at 0.2 keV can vary from 0 to ~ 1000. Thus the model does not rule out the possibility of significant differences in the strength and temperature of the big bumps from source to source. It does suggest however that the correlations observed are not due to changing big bump parameters (i.e. neither the strength nor temperature) but that they are consistent with the effects of absorption by dusty cold gas.

The big bump may be produced by an AD with a surrounding hot corona, an optically-thin gas or perhaps reprocessing in cool clouds. The absorber is cold gas with an approximately Galactic dust abundance and its column density varies from 0 to $\sim 4 \times 10^{21}$ cm^{-2}. The distribution of the intrinsic N_H in the RIXOS AGN implied by the modelling suggests a high covering factor, e.g. a toroidal or spherical geometry of the gas. The presence of dust places it beyond the BLR and, if it is toroidal, then the different types of observed continua may be due to an orientation effect with the column density increasing with the viewing angle.

If the obscuring torus which lies between the BLR and the NLR is responsible for the absorption, then the column density of the clouds which make up the torus must be significantly lower than that observed in Seyfert 2s. We speculate that the rarity of 'type 2' quasars is due to obscuring tori with low column densities which do not always fully absorb the BLR; this may be a physical consequence of the high luminosity in quasars compared to Seyferts. An alternative source of the absorbing gas may be the bulge of a spiral host galaxy or an elliptical host galaxy.

REFERENCES

Allen S. W., Fabian A. C., 1992, MNRAS, 258, L29

Antonucci R., 1993, Ann. Rev. Astron. Astrophys., 31, 473

Antonucci R., Kinney A., Ford H., 1989, ApJ, 342, 64

Arnaud K. A., Branduardi-Raymont G., Culhane J. L., Fabian A. C., Hazard C., McGlynn T. A., Shafer R. A., Tennant A. F. Ward M. J., 1985, MNRAS, 217, 105

Avni Y., Tananbaum H., 1986, ApJ, 305, 83

Barvainis R., 1993, ApJ, 412, 513

Brandt W. N., Fabian A. C., Pounds K. A., 1996, MNRAS, 278, 326

Cardelli J. A., Clayton G. C., 1991, AJ, 101, 1021

Cardelli J. A., Clayton G. C., Mathis J. S., 1989, 345, 245

Cash J., 1979, ApJ, 228, 939

Clavel J. et al. , 1991, ApJ, 366, 64

Comastri A., Setti G., Zamorani G., Elvis M., Giommi P., Wilkes B., McDowell J. C., 1992, ApJ, 384, 62

Czerny, B., Elvis, M. 1987, ApJ, 321, 305

Edelson R. A., Malkan M. A., 1986, ApJ, 308, 509

Elvis M., Lockman F. J., Wilkes B. J., 1989, AJ, 97, 777

Elvis M., Wilkes B., McDowell J. C., Green R. F., Bechtold J., Willner S. P., Oey M. S., Polomski E., Cutri R., 1994, ApJS, 95,1

Ferland, G. J., Rees, M. J. 1988, ApJ, 332, 141

Fiore F., Elvis M., Siemiginowska A., Wilkes B. J., McDowell J. C., Mathur S., 1995, ApJ, in press (expected Aug 10)

Francis P. J., Hewett P. C., Foltz C. B., Chaffee F. H., Weymann R. J., Morris S. L., 1991, ApJ, 373, 465

Gioia, I. M., Maccacaro, T., Schild, R. E., Stocke, J. T., Morris, S. L., Henry, J. P., 1990, ApJS, 72, 567

Gorenstein P., 1975, ApJ, 198, 40

Guilbert, P. W., Rees, M. J. 1988, MNRAS, 233, 475

Hasinger, G., Boese, G., Predehl, P., Turner, T. J., Yusaf, R., George, I. M., Rohrbach, G., 1994, Journal of the High Energy Astrophysics Science Arcive Research Center, 4, 40

Kinney A. L., Huggins P. J., Glassgold A. E., Bregman N. J., 1987, ApJ, 314, 145

Koratkar A. P., Kinney A., Bohlin R. C., 1992, ApJ, 400, 435

Krolik J. H., Begelman M. C., 1988, ApJ, 329, 702

Laor A., Draine B. T., 1993, ApJ, 402, 441

Laor A., Fiore F., Elvis M., Wilkes B. J., McDowell J. C., 1994, ApJ, 435, 611

Madau, P. 1988, ApJ, 327, 116

Mason K. O. et al. , 1996, in preparation

Mathis J. S., Cardelli J. A., 1992, ApJ, 398, 610

Mathur S., Wilkes B., Elvis M. & Fiore F., 1994, ApJ, 434, 493

Miller J. S., Goodrich R., 1987 Bull AAS, 18, 1001

Mittaz J. P. D. et al. , 1996, in preparation

Morrison R., McCammon D., 1983, ApJ, 270, 119

Mushotzky R. F., 1984, Advances in Space Research, 3, 10-13, 157

Mushotzky R. F., Done C., Pounds K. A., 1993, Ann. Rev. Astron. Astrophys., 31, 717

Nandra K., George I. M., 1994, MNRAS, 267, 974

Neugebauer G., Green R. F., Matthews K., Schmidt M., Soifer B. T., Bennet J,. 1987, ApJS, 63, 615

O'Brien P.T., Gondhalekar P.M., Wilson R., 1988, MNRAS, 233, 801

Pfefferman E. et al. , 1986, Proc. SPIE, 733, 519

Pringle J. E., 1981, Ann. Rev. Astron. Astrophys., 22, 471

Puchnarewicz E. M., Mason, K. O., Córdova, F. A., Kartje, J., Branduardi-Raymont, G., Mittaz, J. P. D., Murdin, P. G., Allington-Smith, J., 1992, MNRAS, 256, 589

Puchnarewicz E. M., Mason K. O., Córdova F. A., 1994, MNRAS, 270, 663

Puchnarewicz E. M., Mason K. O., Siemiginowska A., Pounds K. A., 1995, MNRAS, 276, 20

Puchnarewicz E. M. et al. , 1996, in preparation (Paper 2)

Rao S., Briggs F., 1993, ApJ, 419, 515

Reichert G. A., Mason K. O., Thorstensen J. R., Bowyer S., 1982, ApJ, 260, 437

Ryter C., Cesarsky C. J., Audouze J., 1975, ApJ, 198, 103

Stark, A. A., Gammie, C. F., Wilson, R. F., Ball, J., Linke, R. A., Heiles, C., Hurwitz, M., 1992, ApJS, 79, 77

Stocke, J. T., Morris, S. L., Fleming, T. A., Gioia, I. M., Maccacaro, T., Schild, R., Wolter, A., Patrick, H. J., 1991, ApJS, 76, 813

Sun W.-H. Malkan M. A., 1989, ApJ, 346, 68

Tananbaum, H., et al. , 1979, ApJ, 234, L9

Thompson R. J., Córdova F. A., 1994, ApJ, 434, 54

Turner, T. J., Pounds, K. A., 1989, MNRAS, 240, 833

Ulrich M.-H., Molendi S., 1996, ApJ, in press

Walter, R., Fink, H. H., 1993, A& A, 274, 105 (WF)

Wilkes B., Tananbaum H., Worrall D. M., Avni Y., Oey M. S. & Flanagan J., 1994, ApJS, 92, 53

Wills B. J., Netzer H., Wills D., 1985, ApJ, 288, 94

Zheng W., Malkan M A., 1993, ApJ, 415, 517